Analytical Excited-State Gradients and Derivative Couplings in TDDFT with Minimal Auxiliary Basis Set Approximation and GPU Acceleration

Zhichen Pu¹, Xiaojie Wu¹, Yuanheng Wang¹, Cheng Fan^{1,2}, Wen Yan¹, Zehao Zhou^{1,3,*}, Yi Qin Gao^{2,*}, Qiming Sun^{1,*}

¹ByteDance Seed, ²New Cornerstone Science Laboratory, College of Chemistry and Molecular Engineering, Peking University, Beijing 100871, China, ³Zhongguancun Academy

*Corresponding authors

Abstract

Calculating excited-state gradients and derivative couplings using time-dependent density functional theory (TDDFT) remains a computationally demanding task. An efficient variant, TDDFT with resolution of the identity and a minimal auxiliary basis (TDDFT-ris), has been developed to accelerate excitation energy calculations. However, the formulation and implementation of analytical derivatives for this method have not yet been reported. In this work, we present an implementation of analytical excited-state gradients and derivative couplings within the TDDFT-ris framework. Benchmark calculations on medium-sized organic molecules demonstrate a two-to three-fold speedup for both gradients and derivative couplings compared to standard TDDFT. The accuracy of the TDDFT-ris approach is assessed for gradient-dependent applications, including geometry optimizations, emission energy calculations, and the localization of minimum-energy crossing points. Overall, the TDDFT-ris method provides reliable approximations for most cases, with noticeable errors mainly occurring in derivative couplings between nearly degenerate states.

Date: November 26, 2025

Correspondence: Qiming Sun at qiming.sun@bytedance.com, Zehao Zhou at zhouzehao@bjzgca.edu.cn, Yiqin Gao at gaoyq@pku.edu.cn

1 Introduction

Excited states play a crucial role in the study of photochemistry, electronic spectroscopy, non-adiabatic processes, electronic transitions, energy transfer, and charge transfer problems. The computation of excited-state gradients within time-dependent density functional theory (TDDFT) is crucial for excited-state geometry optimization, enabling prediction of fluorescence emission wavelengths in molecules. Similarly, derivative couplings (also known as first-order non-adiabatic coupling matrix elements, fo-NACMEs) are essential for simulating molecular dynamics (MD) on excited state potential energy surfaces, particularly when coupled with Fewest Switches Surface Hopping (FSSH) to explore critical regions, such as conical intersections that govern non-radiative decay pathways [24, 69, 70].

The analytical derivatives of excited states can be computed using various wavefunction-based methods, including the equation-of-motion coupled-cluster theory [13, 18, 63, 67], the algebraic diagrammatic construction

(ADC) method[40, 54], selected configuration interaction (CI)[7, 8], state-average multi-configurational self-consistent field methods[15, 33] and multi-reference CI methods[14, 39]. However, these methods are considered computationally demanding and are often unaffordable for medium-sized molecules. Density Functional Theory (DFT)[26, 30] has revolutionized computational chemistry and materials science by providing an efficient and accurate framework to describe the electronic structure of molecules and solids. The Time-Dependent Density Functional Theory (TDDFT) [57] extends DFT to describe electronic excited states. Compared to the wavefunction theories, TDDFT offers a reasonable estimation of excited state energies and analytical derivatives at a more affordable computational cost. The calculation of TDDFT gradients and derivative couplings has been extensively investigated[17, 24, 38, 47, 53, 60, 62, 64, 68, 72, 83–85]. Analytical derivative couplings within the TDDFT framework were developed separately by Li and Zhang, using time-dependent response theory to compute the excited state derivative couplings[23, 37, 38, 62, 83, 84]. Qi et al. also derived similar TDDFT equations based on the time-dependent many-body wavefunction framework [47].

Although TDDFT significantly improves computational efficiency compared to wavefunction-based methods, TDDFT-based MD are still limited to relatively small molecules [24, 42, 65] due to the substantial computational cost of evaluating gradients and derivative couplings. Applying TDDFT derivative computations to large-scale systems with hundreds or thousands of atoms, such as conjugated polymers, biomolecular chromophores, or nanostructured materials, is not feasible on a routine basis. Furthermore, the MD simulation with FSSH schemes requires hundreds of trajectories and thousands steps per trajectory to ensure statistically robust results[41, 48], further increasing the computational demands. Consequently, various approximations and adjustments to the nuclear motion have been employed to estimate the coupling between electrons and nuclei[3, 12, 58, 59, 80].

The primary computational bottleneck in the TDDFT method lies in the calculation of the electron-repulsion integrals within the linear-response kernel. To address this computational challenge, various approximation methods have been developed to balance accuracy and computational efficiency [2, 4, 10, 19, 20, 43, 46, 55, 56, 73, 78, 88]. Some of these approaches have been extended to excited-state gradients [22] and derivative couplings [44, 45, 81]. Semi-empirical two-electron integrals have been used to approximate the linear-response kernel, leading to the development of simplified TDDFT (sTDDFT/sTDA) methods[11, 20]. The minimal auxiliary basis model (TDDFT-as) was proposed to approximate the Coulomb matrix in the linear-response kernel for semi-local density functionals [19]. In this approach, a single s-type Gaussian auxiliary function is used per atom. This minimal auxiliary basis model was extended to the computation of the exchange matrix for the hybrid exchange-correlation functionals by Zhou, introducing the TDDFT-ris method [86, 87]. The TDDFT-ris method achieves a speedup of up to two orders of magnitude compared to conventional TDDFT without compromising accuracy.

Another effective strategy for improving TDDFT computational performance is GPU acceleration [28, 29]. GPU architectures are particularly well suited for tensor operations, making them highly compatible with density-fitting approaches[75]. The density-fitting implementation in GPU4PySCF achieves performance improvements of two to three orders of magnitude over conventional CPU implementations for DFT energies, analytical nuclear gradients, and Hessians[36, 79]. The analytical-derivative module in GPU4PySCF provides general APIs that can be readily extended to excited-state derivative calculations.

Building upon this foundation, this work extends the TDDFT-ris method to compute analytical nuclear gradients and derivative couplings. We will present the theoretical background of TDDFT, the TDDFT-ris method, and their analytical derivatives in Section 2. We will then briefly discuss how the features of standard TDDFT and the TDDFT-ris approximation are implemented with GPU support in Section 3. In Section 4, we evaluate the performance of the TDDFT-ris approximation to determine the performance improvements it offers over standard TDDFT computations. In Section 5, we assess the accuracy of TDDFT-ris gradients and derivative couplings using a series of metrics, including the optimization of excited-state geometries, the transition probabilities between electronic states, and the minimum-energy crossing point (MECP).

2 Theory

In this section, we briefly review the theoretical framework of TDDFT and its extension to the analytical calculation of excited-state gradients and derivative couplings. From this foundation, we derive the TDDFT-ris approximation for the derivative calculations.

2.1 TDDFT gradients and analytical derivative couplings

Within the linear-response TDDFT framework for closed-shell systems, as formulated by Casida[6], the excitation energies are obtained by solving the following generalized eigenvalue problem:

$$\begin{pmatrix} A & B \\ B & A \end{pmatrix} \begin{pmatrix} X_I \\ Y_I \end{pmatrix} = \omega_I \begin{pmatrix} 1 & 0 \\ 0 & -1 \end{pmatrix} \begin{pmatrix} X_I \\ Y_I \end{pmatrix}, \tag{1}$$

$$A_{ai,bj} = (\varepsilon_a - \varepsilon_i)\delta_{ab}\delta_{ij} + K_{ai,bj}, \tag{2}$$

$$B_{ai,bj} = K_{ai,jb}, \tag{3}$$

$$K_{pq,rs} = g_{pq,sr} + (f_{xc})_{pq,sr},\tag{4}$$

$$g_{pq,sr} = (pq|sr) - c_x(pr|sq), \tag{5}$$

$$(f_{xc})_{pq,sr} = \frac{\partial^2 E_{xc}}{\partial D_{qp} \partial D_{rs}},\tag{6}$$

$$(pq|sr) = \iint d\mathbf{r}_1 d\mathbf{r}_2 \frac{p(\mathbf{r}_1)q(\mathbf{r}_1)s(\mathbf{r}_2)r(\mathbf{r}_2)}{|\mathbf{r}_1 - \mathbf{r}_2|},$$
(7)

where the eigenvalue for state I is ω_I , and the eigenvector is $\begin{pmatrix} X_I \\ Y_I \end{pmatrix}$. In Eq. (2), ε is the orbital energy, and

 $K_{pq,rs}$ is the element of the coupling matrix. In this manuscript, we use a,b to denote virtual orbitals, i,j denote occupied orbitals, and p,q,r,s denote dummy orbitals, which can refer to either molecular orbitals or atomic orbitals. The four-center two-electron repulsion integral is denoted as (pq|sr) as defined in Eq. (7). The integral $-c_x(pr|sq)$ from Eq. (5) together with $(f_{xc})_{pq,rs}$ in Eq. (4) jointly form the exchange-correlation (XC) functional kernel, where c_x presents the fraction of exact exchange contribution. The pure functional component, $(f_{xc})_{pq,rs}$, is the second-order derivative of the XC functional E_{xc} with respect to the density matrix \mathbf{D} , as defined in Eq. (6).

The theoretical framework for calculating gradients and derivative couplings within TDDFT is well-established [17, 24, 38, 47, 53, 60, 62, 64, 68, 84]. Following the unified formalism developed by Li and co-workers [37, 38, 74], the derivative coupling between two electronic states, Ψ_I and Ψ_J , is defined as:

$$g_{IJ}^{\xi} = \langle \Psi_I | \frac{\partial}{\partial \xi} | \Psi_J \rangle, \quad \xi \in x = \{ \mathbf{R}_1, \mathbf{R}_2, \dots, \mathbf{R}_N \},$$
 (8)

where ξ is a nuclear coordinate of the N-atom molecule. The indices I and J represent specific electronic states. When I is set to 0, it denotes the ground state. The gradient for state I is defined as

$$\mathbf{g}_{I}^{\xi} = \frac{\partial}{\partial \xi} E_{I},\tag{9}$$

where E_I is the energy of the *I*-th electronic state.

The derivative computation must account for the response of molecular orbitals with respect to the nuclear coordinates. To incorporate this constraint, a Lagrangian[16, 17] is introduced as follows:

$$L[x, \boldsymbol{C}(x), \boldsymbol{Z}, \boldsymbol{W}] = g[x, \boldsymbol{C}(x)] + \sum_{ai} Z_{ai} F_{ai}(x) - \sum_{pq} W_{pq} (S_{pq}(x) - \delta_{pq}), \tag{10}$$

where C(x) represents the molecular orbital coefficients at a given atomic geometry x. Two constraints are enforced via the Lagrange multipliers, Z and W. The constraint $F_{ai}(x) = 0$, associated with Z, corresponds to the stationary conditions of the ground state energy w.r.t. molecular orbital coefficients:

$$F_{ai}(x) = \frac{\partial E_{GS}}{\partial C_{ai}} = 0. \tag{11}$$

The other constraint, $S_{pq}(x) - \delta_{pq} = 0$, ensures the orthonormality of the molecular orbitals.

The core of the Lagrangian (10) is the generating function $g[x, \mathbf{C}(x)]$. Its specific form depends on the property to be calculated [37, 38], and these terms are well-discussed in Ref. 38. For convenience, we list the generating functions here. For the excited-state gradient in TDDFT, it takes the following form:

$$g_I[x, C(x)] = \langle F; T_{II} \rangle + \langle g; \Gamma_{II} \rangle + \langle f_{xc}; \{R_I^S, R_I^S\} \rangle. \tag{12}$$

For the derivative couplings between the ground state and an excited state, or between two excited states, the corresponding forms are

$$g_{0I}[x, \mathbf{C}(x)] = \langle \underline{\mathbf{d}}; \boldsymbol{\gamma}^{0I} \rangle, \tag{13}$$

$$g_{IJ}[x, \mathbf{C}(x)] = (E_J - E_I)^{-1} \left(\langle \mathbf{F}; \mathbf{T}_{IJ} \rangle + \langle \mathbf{g}; \mathbf{\Gamma}_{IJ} \rangle + \langle \mathbf{f}_{xc}; \{\mathbf{R}_I^S, \mathbf{R}_J^S\} \rangle \right) + \langle \underline{\mathbf{d}}; \gamma^{IJ} \rangle. \tag{14}$$

We follow the notations of Ref. 38 for the matrices and symbols used in Eqs. (12) to (14), which are also summarized in the Appendix A.1 for quick reference. It should be noted that the quadratic-response term is neglected, following the recommendation in Ref. 74.

Finally, we directly list the final expressions for the excited-state gradient and derivative couplings between the ground state and excited states, or between excited states

$$g_I^{\xi} = \langle \boldsymbol{H}^{(\xi)}; \boldsymbol{P}_I \rangle + \langle \boldsymbol{g}^{(\xi)}; \{\boldsymbol{D}, \boldsymbol{P}_I\} + \Gamma_{II} \rangle + \langle \boldsymbol{v}_{xc}^{(\xi)}; \boldsymbol{P}_I \rangle + \langle \boldsymbol{f}_{xc}^{(\xi)}; \{\boldsymbol{R}_I^S, \boldsymbol{R}_I^S\} \rangle - \langle \boldsymbol{S}^{(\xi)}; \boldsymbol{W} \rangle.$$
(15)

$$g_{0I}^{\xi} = \langle \boldsymbol{H}^{(\xi)}; \boldsymbol{Z}^{S} \rangle + \langle \boldsymbol{g}^{(\xi)}; \{\boldsymbol{D}, \boldsymbol{Z}^{S}\} \rangle + \langle \boldsymbol{v}_{xc}^{(\xi)}; \boldsymbol{Z}^{S} \rangle - \langle \boldsymbol{S}^{(\xi)}; \boldsymbol{W} \rangle + \langle \boldsymbol{d}^{(\xi)}; \boldsymbol{\gamma}^{0I} \rangle.$$
(16)

$$g_{IJ}^{\xi} = (E_J - E_I)^{-1} \tilde{L}_{IJ}^{(\xi)},\tag{17}$$

$$\tilde{L}_{IJ}^{(\xi)} = \langle \boldsymbol{H}^{(\xi)}; \boldsymbol{P}_{IJ} \rangle + \langle \boldsymbol{g}^{(\xi)}; \{\boldsymbol{D}, \boldsymbol{P}_{IJ}\} + \Gamma_{IJ} \rangle
+ \langle \boldsymbol{v}_{xc}^{(\xi)}; \boldsymbol{P}_{IJ} \rangle + \langle \boldsymbol{f}_{xc}^{(\xi)}; \{\boldsymbol{R}_{I}^{S}, \boldsymbol{R}_{I}^{S}\} \rangle - \langle \boldsymbol{S}^{(\xi)}; \tilde{\boldsymbol{W}} \rangle + \langle \boldsymbol{d}^{(\xi)}; \tilde{\boldsymbol{\gamma}}^{IJ} \rangle.$$
(18)

The matrix Z is determined by solving the so-called Z-vector equation [21]

$$(\mathbf{A} + \mathbf{B})\mathbf{Z} = g^{(\text{VO})} - g^{(\text{OV})}. \tag{19}$$

The notations used in Eqs. (15) to (19) are defined in Appendix A.2. The right-hand side of the Z-vector equation (19) depends on the specific property being calculated. For further details, the reader is referred to Ref. 38.

2.2 Excited-state gradient and derivative couplings for TDDFT-ris

The most computationally demanding step in solving the TDDFT Casida equation (1) is the evaluation of the coupling matrix K (4). It involves the evaluation of two-electron integrals and the numerical integration of the XC kernel. To reduce the computational cost of the coupling matrix evaluation, the TDDFT-ris method employs the resolution of identity (RI) with a small auxiliary basis set to approximate the two-electron integrals within the coupling matrix. Additionally, this method neglects the contribution from the pure XC functional kernel, *i.e.*,

$$K_{pq,rs} \approx K_{pq,rs}^{\text{ris}} = g_{pq,sr}^{\text{ris}}, \tag{20}$$

$$g_{pq,sr}^{\text{ris}} = \sum_{AB} (pq|A)(\mathbf{M}^{-1})_{AB}(B|sr) - c_x \sum_{AB} (pr|A)(\mathbf{M}^{-1})_{AB}(B|sq), \tag{21}$$

$$M_{AB} = (A|B), (22)$$

where A and B denote auxiliary basis functions, while (A|B) and (pq|A) represent the two-center and three-center two-electron repulsion integrals, respectively.

The auxiliary basis set comprises a single Gaussian-type orbital (GTO) for each angular momentum component (up to l = 2) on each atom. The use of a minimal auxiliary basis set for the RI approximation introduces

larger errors compared to the regular density fitting approximation with optimized JK-fit auxiliary basis sets. In the TDDFT-ris scheme, distinct auxiliary basis sets can be employed for the Coulomb (J-fit) and exchange (K-fit) integrals, corresponding to the first and second terms in Eq. (21), respectively. The exponents of these auxiliary GTOs are determined by minimizing the deviation of the resulting total excitation energies from standard TDDFT reference values [87].

Within the TDDFT-ris formalism, only the generating functions in Eq. (10) are modified as follows:

$$g_I = \langle \mathbf{F}; \mathbf{T}_{II} \rangle + \langle \mathbf{g}^{ris}; \mathbf{\Gamma}_{II} \rangle,$$
 (23)

$$g_{IJ} = (E_J - E_I)^{-1} \left(\langle \mathbf{F}; \mathbf{T}_{IJ} \rangle + \langle \mathbf{g}^{ris}; \mathbf{\Gamma}_{IJ} \rangle \right) + \langle \underline{\mathbf{d}}; \boldsymbol{\gamma}^{IJ} \rangle. \tag{24}$$

In contrast, the generating functions for the derivative couplings between the ground and excited states remain identical to those in standard TDDFT (13). The excited-state gradient and derivative couplings are computed as

$$g_{I}^{\xi} = \langle \boldsymbol{H}^{(\xi)}; \boldsymbol{P}_{I} \rangle + \langle \boldsymbol{g}^{(\xi)}; \{\boldsymbol{D}, \boldsymbol{P}_{I}\} \rangle + \langle \boldsymbol{g}^{\mathrm{ris},(\xi)}; \boldsymbol{\Gamma}_{II} \rangle + \langle \boldsymbol{v}_{\mathrm{xc}}^{(\xi)}; \boldsymbol{P}_{I} \rangle - \langle \boldsymbol{S}^{(\xi)}; \boldsymbol{W} \rangle,$$

$$g_{IJ}^{\xi} = (E_{J} - E_{I})^{-1} \left(\langle \boldsymbol{H}^{(\xi)}; \boldsymbol{P}_{IJ} \rangle + \langle \boldsymbol{g}^{(\xi)}; \{\boldsymbol{D}, \boldsymbol{P}_{IJ}\} \rangle + \langle \boldsymbol{g}^{\mathrm{ris},(\xi)}; \boldsymbol{\Gamma}_{IJ} \rangle + \langle \boldsymbol{v}_{\mathrm{xc}}^{(\xi)}; \boldsymbol{P}_{IJ} \rangle \right)$$

$$-\langle \boldsymbol{S}^{(\xi)}; \tilde{\boldsymbol{W}} \rangle + \langle \boldsymbol{d}^{(\xi)}; \tilde{\boldsymbol{\gamma}}^{IJ} \rangle \right).$$

$$(25)$$

It should be noted that the RI approximation in TDDFT-ris does not modify every term that involves two-electron integrals or exchange—correlation (XC) kernel integration. The right-hand side of the Z-vector equation (19) within the TDDFT-ris framework is updated according to the specific property being calculated (see Appendix A.3 for details). The left-hand side of the Z-vector equation is identical to that in standard TDDFT, as these tensors originate from the orbital response of the ground-state calculation.

To mitigate errors in the TDDFT-ris scheme, distinct auxiliary basis sets can be utilized for the J-fit and K-fit terms. Upon extending the TDDFT-ris method to the calculation of analytical gradients and derivative couplings, certain derivative integrals $g^{(\xi)}$ in Eqs. (15) and (18) are replaced by their TDDFT-ris counterparts, $g^{\text{ris},(\xi)}$, as shown in Eqs. (25) and (26). The derivatives of the two-electron integrals are evaluated as follows:

$$\frac{\partial}{\partial \xi} \left[\sum_{AB} (pq|A)(\mathbf{M}^{-1})_{AB}(B|sr) \right] = \sum_{AB} (pq|A)^{\xi} (\mathbf{M}^{-1})_{AB}(B|sr) + \sum_{AB} (pq|A)(\mathbf{M}^{-1})_{AB}(B|sr)^{\xi} - \sum_{ABCD} (pq|A)(\mathbf{M}^{-1})_{AC} \mathbf{M}_{CD}^{\xi} (\mathbf{M}^{-1})_{DB}(B|sr). \tag{27}$$

3 Implementation

The program for calculating TDDFT gradients and derivative couplings for both standard TDDFT and the approximate TDDFT-ris methods has been developed within the GPU4PySCF package[32, 36, 51, 66, 79]. In this TDDFT derivative program, we have integrated various methods for calculating two-electron integrals and their gradients, including density fitting approximations and exact analytical integral evaluations. Two-electron integrals and their derivatives are evaluated using the GPU4PySCF integral implementations[36, 79]. The high-order derivatives of the XC functionals are evaluated using the LibXC library[31]. We will not discuss the details of these integral evaluation algorithms in this work, as they are beyond the scope of this study. The source code for excited-state gradients and derivative couplings for both TDDFT and TDDFT-ris is publicly available in the GPU4PySCF GitHub repository at https://github.com/pyscf/gpu4pyscf. Our implementation is validated via finite-differences as shown in Appendix B.

To simplify the code management across multiple TDDFT variants, our current program implementation integrates TDDFT and its counterpart within the Tamm-Dancoff Approximation [25] (TDA) into a unified code framework. In this setup, TDA gradients and derivative couplings are evaluated using the TDDFT routines by setting the \boldsymbol{Y} amplitudes to zero. A similar hierarchical structure and implementation strategy is also employed for the TDDFT-ris and TDA-ris methods.

The TDDFT and its derivative code is initially implemented using exact integral computation routines. Subsequently, density fitting with regular JK-fit auxiliary basis sets is introduced. The three-center integral tensors and their derivatives required by the density fitting algorithms are often too large to be fully stored in GPU memory. Consequently, these tensors are divided into small batches, along either the atomic orbital dimension or the auxiliary basis dimension, and are evaluated in multiple passes. When computing the derivatives, nested loops over these batches are encountered, which results in some tensors being recomputed and generated multiple times. This could lead to a relatively high overhead in density fitting TDDFT derivative computations for large molecules.

The TDDFT-ris implementation is based on the density-fitting variant, except that the auxiliary basis sets are replaced by those specific to TDDFT-ris. The parameters for the J-fit and K-fit basis sets are identical and were optimized to minimize errors in excitation energies.[87]. The three-index integral tensor in the TDDFT-ris method is significantly smaller than its counterpart in the density-fitting TDDFT program. These tensors can be transformed into the molecular orbital representation, retaining only the specific necessary occupied-occupied and occupied-virtual blocks to further reduces their sizes. Additionally, the molecular orbital space can be truncated to reduce computational and storage costs. However, in the calculations presented in this work, all molecular orbitals were included. This reduced-size integral storage scheme is employed during the calculation of excitation energies.

For the calculation of integral derivatives, it is possible to perform a partial transformation for one or two indices of the three-index integral tensors to reduce memory usage and avoid the recomputation of certain intermediates. However, this alternative scheme would require a distinct code architecture and memory management strategy. In our current implementation, we did not pursue alternative schemes for the TDDFT-ris method in derivative coupling and gradients computational programs. This is because the evaluation of integral derivatives is not the computationally dominant step in these calculations, as will be demonstrated in the subsequent section.

The TDDFT amplitudes and molecular orbital coefficients are inherently subject to phase ambiguity, which can lead to uncertain phases in the derivative couplings. Proper phase handling is essential when tracking the geometric evolution of the system in molecular dynamics simulations. To ensure phase consistency along a geometric path, we developed a phase-determination function that sets the phase based on the overlap of the excited-state wavefunction with the previous step. In our implementation, the overlap is computed using the five most dominant contributing determinants.

4 Benchmark

In this work, the auxiliary basis set employed in the TDDFT-ris method is composed of s- and p-type orbitals for Coulomb integrals, while only s-type orbitals are used for the exchange integrals. The exponents of the auxiliary Gaussian functions for each atomic type are adopted from Ref. 87, where they are optimized for the PBE0 [1] XC functional in conjunction with the def2-TZVP [76] basis set. For the density fitting approximation in the remaining components, the def2-universal-JKFIT auxiliary basis [75] is utilized.

Although minor discrepancies exist between the results of TDDFT and TDA, this does not influence our comparison of the TDDFT-ris accuracy against that of standard TDDFT calculations. Similarly, the systematic difference in computational speed between TDA and TDDFT does not impact our performance analysis of the TDDFT-ris method. Consequently, unless otherwise specified, all calculations are performed using the TDA at the PBEO/def2-TZVP level of theory.

The molecules used for the benchmarks are selected from the benchmark systems included within the GPU4PySCF package. These molecules and their corresponding system sizes are detailed in Table 1. All calculations are performed on a single compute node equipped with 6 CPU cores, 30 GB of system memory, and a single NVIDIA Tesla V100 GPU.

4.1 Performance Benchmark

The performance for excited state energy computations, gradients, and derivative couplings calculations using the TDA-ris and TDA approaches is illustrated in Figures 1a (exact integrals) and 1b (density fitting). To

Table 1 Molecules used in computational performance tests.

Molecule	Number of atoms	Number of orbitals
Vitamin C	20	420
Inosine	31	661
Bisphenol A	33	623
Mg Porphin	37	848
Penicillin V	42	858
Ochratoxin A	45	951
Cetirizine	52	993
Tamoxifen	57	1042
Raffinose	66	1246
Sphingomyelin	84	1335

clearly demonstrate the cost of the excited state computations, the computational time for the underlying Self-Consistent Field (SCF) calculation is also provided for reference.

In general, each individual derivative of the excited states consumes 5 to 10 times the cost of the ground state SCF computation. Owing to the omission of the XC kernel and the aggressive approximation of two-electron integrals, the TDA-ris method offers substantial acceleration for excited-state energy calculations. Compared to TDA computations with density fitting or exact integrals, the TDA-ris method achieves speed-up factors of 16 and 343, respectively. Regarding the derivative computations, however, the performance gains of the TDA-ris method are considerably diminished.

Among the derivative computation tasks, no acceleration is observed for the calculation of the ground-to-excited state derivative coupling, g_{12}^{ξ} . A modest speed-up is observed in the benchmark tests for the excited-state-to-excited-state derivative coupling, g_{12}^{ξ} , and the excited-state gradient, g_{1}^{ξ} . When the two-electron integrals for the ground state are approximated using regular density fitting (Figure 1b), the speed-ups of the TDA-ris method are 2.3 and 2.4, respectively. When exact integrals are employed (Figure 1a), the acceleration achieved by the TDA-ris approximation is reduced to 1.6 and 1.5, respectively.

To understand the large performance difference between derivative coupling and excitation energy calculations, we profiled the derivative calculations using both the standard TDDFT and TDDFT-ris implementations. The computational cost of these calculations arises mainly from three components: solving the Z-vector equations, evaluating the exchange–correlation (XC) functional terms, and computing the derivatives of the Coulomb and exchange integrals. Table 2 presents an example of this profiling for the cetirizine molecule, where the two-electron integrals were evaluated using the density-fitting approximation. For g_{01}^{ξ} , the computational time for each component and the total time are nearly identical between the standard TDA and TDA-ris methods. This is an expected outcome, as this calculation does not involve any terms that are approximated by the TDA-ris auxiliary integrals. The generating function, Eq. (13), and the resulting Lagrangian, Eq. (10), are identical to those within the standard TDA framework; consequently, an identical computational procedure is employed for g_{01}^{ξ} by both TDA and TDA-ris methods. The speed-up for g_{12}^{ξ} and g_1^{ξ} originates from the accelerated evaluation of XC functional terms and the computation of derivatives of Coulomb and exchange integrals.

Standard TDDFT derivative calculations for g_{12}^{ξ} and g_{1}^{ξ} are exceptionally time-consuming, primarily because the requisite third-order derivatives of the XC functionals are currently computed on CPUs. The transition of the XC computations from CPU to GPU is hampered by unresolved implementation issues related to third-order derivatives. Once these issues are resolved, an overall performance improvement of approximately a factor of two can be expected. The TDA-ris method exhibits negligible computational cost for the XC part, as it circumvents the need for third-order derivatives and the computation is completely performed on GPUs.

While the TDA-ris method does provide a speed-up in the calculation of Coulomb and exchange integral derivatives compared to standard TDDFT, the improvement is moderate. This is because the minimal basis RI approximation in TDA-ris applies to a subset of the terms in this computational step. As shown in Eqs. (25)

and (26), many terms remain unchanged and do not benefit from the TDA-ris scheme. Furthermore, when evaluating derivatives of the TDDFT Lagrangian (10), it is necessary to compute the ground-state orbital response with respect to nuclear coordinates exactly. This orbital response is independent of the TDDFT linear-response matrix. The integral approximation in TDA-ris only reduces the cost associated with the linear-response matrix and the relevant integral derivatives; *i.e.*, solving the Z-vector equations does not benefit from the TDA-ris scheme. As shown in Table 2, in a typical nuclear gradient calculation, integral derivatives account for roughly 30% of the computational effort, while solving the Z-vector equations for the ground-state orbital response consumes approximately 60% of the total cost. Consequently, the computational advantage of the TDA-ris framework diminishes for these higher-order properties.

The scaling of computational time with respect to system size for the TDA-ris excitation energy, derivative coupling, and excited-state gradient calculations is presented in Figure 2. The evaluations of the derivative coupling and gradient constitute the rate-determining steps of the overall procedure, with computational costs that far exceed those of the SCF and TDA-ris energy calculations. Considering the requirements of surface-hopping molecular dynamics that employs TDDFT as the electronic structure solver, the dominant expense arises from the computation of excited-state gradients and derivative couplings. Employing the TDA-ris approximation could result in an overall twofold acceleration.

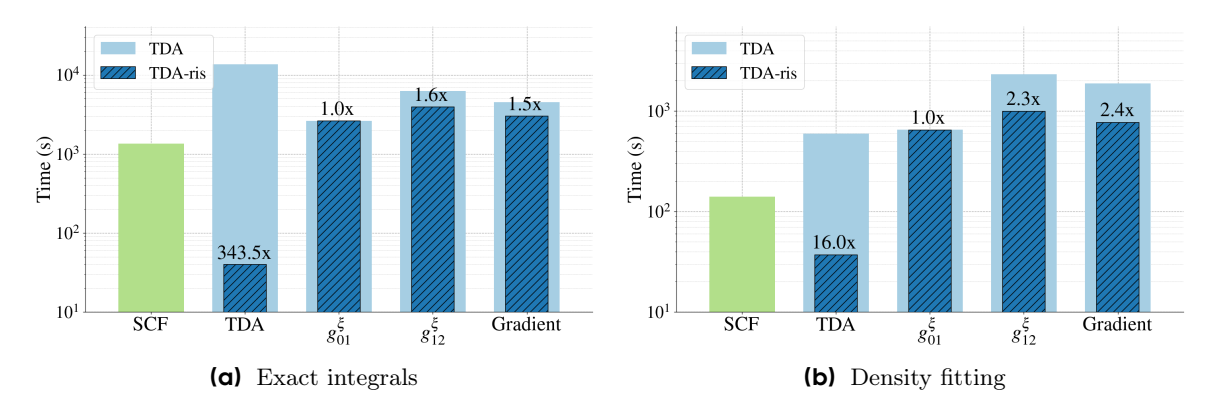


Figure 1 Performance comparison of the TDA-ris and standard TDA methods for calculating the SCF energy, excitation energy, derivative couplings (g_{01}^{ξ} and g_{12}^{ξ}), and excited-state gradient based on the total computational time for the molecules listed in Table 1. The two-electron integrals in the ground state and Z-vector equations are evaluated with (a) the exact algorithm and (b) density fitting approximation.

4.2 Ris approximation for Z-vector Solver

Handling the orbital response exactly in derivative calculations limits the performance gains of the TDDFT-ris method. One might wonder whether the Z-vector equations can be accelerated using an approach analogous to TDDFT-ris by applying an approximation to the integrals in the ground-state orbital response. In this scheme, the approximation in Eq. (20) is applied to the terms within the (A+B) matrix of Eq. (19) during the evaluation of derivative properties. We test this approximation for the Z-vector equations in the calculation of excited-state gradients for the molecules listed in Table 1. Table 3 summarizes the computational performance and accuracy of this approach compared to the standard TDA-ris method. The results indicate that the ris-approximated Z-vector solver substantially reduces computational time, achieving an acceleration of approximately four- to five-fold for calculations with exact integrals and two- to three-fold when density fitting is employed. The deviations in the calculated gradients are generally small.

However, approximating the orbital response in this scheme affects only the gradients and derivative couplings, not the excitation energies. This may disrupt the consistency between energies and derivatives. Such inconsistencies can slow down the convergence of geometry optimizations or violate energy conservation in molecular dynamics simulations. Given the significant performance gains, we will investigate in our future work whether applying the ris-approximation to the Z-vector solver is suitable for more complex systems and a wider range of properties.

Table 2 Breakdown of computational time (in seconds) for the most computationally intensive tasks in property calculations of TDA and TDA-ris methods. The two-electron integrals in the ground state and Z-vector equations are calculated with the density fitting approximation.

Computational Task	Property	TDA	TDA-ris
	$egin{array}{c} oldsymbol{g}_{01}^{\xi} \ oldsymbol{g}_{12}^{\xi} \ oldsymbol{g}_{1}^{\xi} \end{array}$	48.8	46.6
Solving Z -vector equations	$\boldsymbol{g}_{12}^{\hat{\boldsymbol{\xi}}}$	61.8	62.1
	\boldsymbol{g}_1^ξ	54.0	54.2
	$egin{array}{c} oldsymbol{g}_{01}^{\xi} \ oldsymbol{g}_{12}^{\xi} \ oldsymbol{g}_{1}^{\xi} \end{array}$	2.2	2.3
Calculation of XC terms	$\boldsymbol{g}_{12}^{\xi}$	121.2	2.7
	\boldsymbol{g}_1^ξ	119.2	2.7
Derivatives of Coulomb and exchange	$egin{array}{c} oldsymbol{g}_{01}^{\xi} \ oldsymbol{g}_{12}^{\xi} \ oldsymbol{g}_{1}^{\xi} \end{array}$	19.9	20.3
integrals	$\boldsymbol{g}_{12}^{\xi}$	70.1	36.8
mograns	\boldsymbol{g}_1^ξ	30.8	19.5
	$egin{array}{c} oldsymbol{g}_{01}^{\xi} \ oldsymbol{g}_{12}^{\xi} \ oldsymbol{g}_{1}^{\xi} \end{array}$	74.8	73.5
Total time	$\boldsymbol{g}_{12}^{\xi}$	267.5	110.5
	\boldsymbol{g}_1^ξ	215.4	85.3

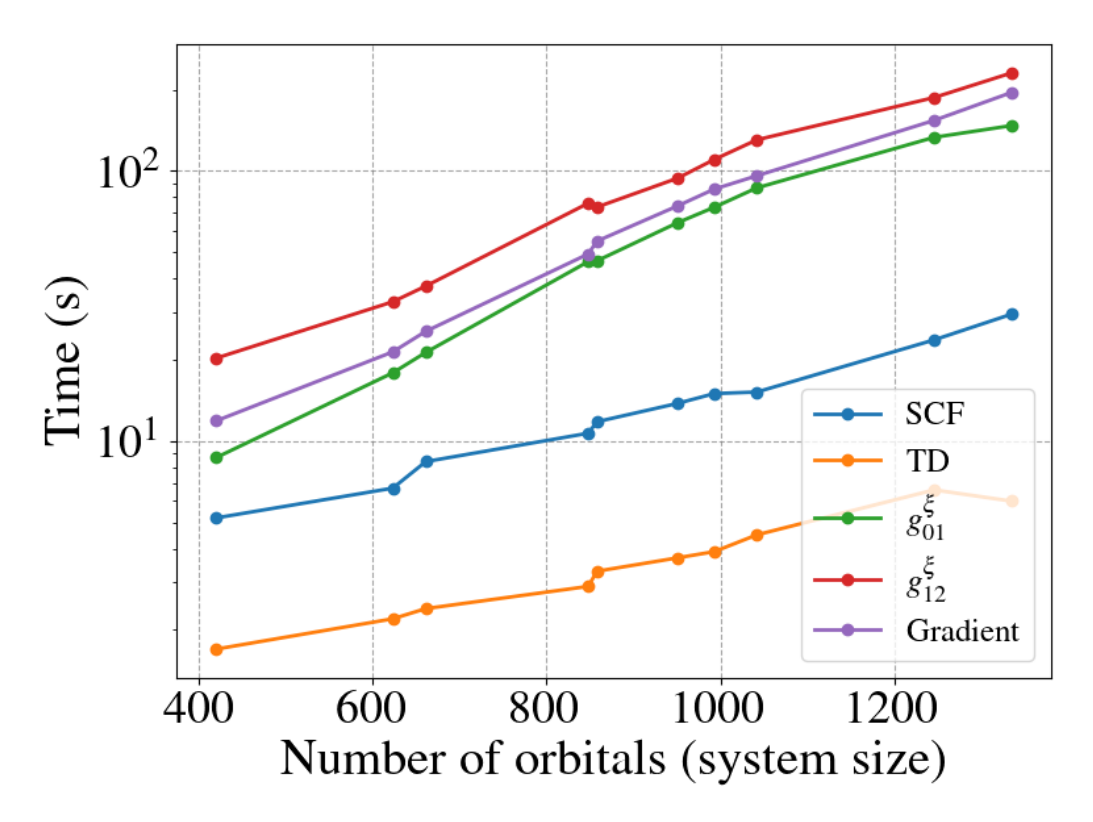


Figure 2 Scaling of the computational cost for the different stages in a TDA-ris calculation with respect to system size (number of basis functions). The density fitting approximation is employed for the ground state and Z-vector computations.

Table 3 Comparison of computational time (s) and gradient deviations (Hartree/Bohr) for the TDA-ris (standard) and TDA-ris with ris-approximated Z-vector solver (ris solver) methods.

Molecule	Time (exact integrals)		Time (density fitting)		Deviation	
	standard	ris solver	standard	ris solver	MAD	RMS
Vitamin C	65.7	18.5	11.9	8.3	6.36×10^{-4}	1.03×10^{-3}
Inosine	159.7	34.3	25.5	12.9	5.15×10^{-4}	1.64×10^{-3}
Bisphenol A	142.5	34.9	21.4	12.4	2.63×10^{-4}	4.41×10^{-4}
Mg Porphin	320.8	68.2	49.3	21.2	7.37×10^{-5}	9.86×10^{-5}
Penicillin V	324.0	62.8	55.0	21.1	2.91×10^{-4}	5.08×10^{-4}
Ochratoxin A	386.0	69.7	74.3	25.5	2.96×10^{-4}	4.88×10^{-4}
Cetirizine	447.5	88.8	85.7	29.4	5.36×10^{-4}	9.73×10^{-4}
Tamoxifen	375.6	78.4	96.0	31.2	1.06×10^{-4}	1.80×10^{-4}
Raffinose	405.7	91.9	153.9	45.7	3.69×10^{-4}	8.98×10^{-4}
Sphingomyelin	400.5	91.4	195.2	49.5	3.34×10^{-4}	1.01×10^{-3}

5 Applications and discussion

In this section, we evaluate the practical applicability of the derivative computation for the TDA-ris method by testing the errors it introduces in comparison to standard TDDFT methods. Properties that are frequently utilized in excited-state studies include potential energy surfaces and the interactions of electronic and nuclear motion through non-adiabatic couplings.

To evaluate the reliability of the TDA-ris method for describing the potential energy surface, a series of tests are performed to locate the optimized geometry of the first excited state and to calculate the corresponding emission energy. To assess the quality of the non-adiabatic couplings, we calculate the derivative couplings, which are the key quantities that govern the transition probabilities between electronic states. These calculations are performed within the framework of the FSSH methodology[69, 70]. Additionally, the MECPs are computed to evaluate the reliability of the derivative couplings obtained from the TDA-ris method.

5.1 Excitation State Geometry Optimization and Emission Energy

This investigation focuses on the first singlet excited state (S_1) , irrespective of molecular symmetry. The test set comprises a diverse range of molecules, with initial geometries taken from Refs. 61 and 71. The Results are summarized in Table 4 and Figure 3.

A close agreement in the emission energies of S_1 between the two approaches is observed across the entire set of test molecules, as shown in Figure 3, where TDA-ris emission energies are plotted against their TDA counterparts. The data points lie closely along the diagonal (y = x), indicating minimal systematic deviation and a strong linear relationship. The emission energies for each molecule from both methods are detailed in Table 4.

To evaluate the quality of the optimized S_1 geometries, two metrics are employed. The first is gradient consistency, defined as the norm of the TDA gradient calculated at the TDA-ris optimized geometry and vice versa. Perfect gradient consistency would yield a zero norm, indicating that the two methods would be able to converge to the same equilibrium geometry under a gradient descent optimization. As shown in Table 4, these gradient norms are consistently small, on the order of 10^{-3} Hartree/Bohr. This finding indicates that a geometry optimized with one method lies in close proximity to a stationary point on the S_1 potential energy surface of the other method.

The second metric involves direct structural comparisons between the optimized geometries, quantified by the mean absolute difference (MAD) and root-mean-square (RMS) difference. For all tested molecules, these deviations are small, demonstrating that TDA-ris produces optimized first excited-state structures highly consistent with those from the standard TDA method.

In summary, the results indicate that the TDA-ris method yields emission energies and optimized geometries that are in strong agreement with those obtained from the standard TDA method. This level of agreement substantiates the use of TDA-ris as a reliable and efficient method for computationally demanding tasks, such as geometry optimizations in fluorescence studies. Nevertheless, a degree of caution is warranted, as we occasionally observe that the TDA-ris approximation can alter the energetic ordering of excited states. Consequently, it is crucial to verify that the state of interest in a TDA-ris calculation corresponds to the correct electronic state within the standard TDA framework, particularly in systems with a high density of states. Despite this minor limitation, the performance benefits justify the application of the method.

Table 4 Comparison of TDA and TDA-ris for excited-state emission energies and excited-state geometries.

Molecule	Emissio	n energy (eV)	Gradients consistency ^a		Geometry consistency ^b	
Molecule	TDA	TDA-ris	TDA-ris	TDA	Geom. MAD	Geom. RMS
acetamide	4.53	4.38	2.89×10^{-3}	2.83×10^{-3}	1.79×10^{-3}	2.86×10^{-3}
acetone	3.81	3.62	1.29×10^{-3}	1.36×10^{-3}	2.08×10^{-3}	3.18×10^{-3}
adenine	3.85	3.79	4.10×10^{-3}	4.11×10^{-3}	5.94×10^{-4}	8.80×10^{-4}
benzene	5.32	5.29	2.31×10^{-3}	2.32×10^{-3}	3.54×10^{-4}	4.95×10^{-4}
benzoquinone	2.39	2.23	2.40×10^{-3}	1.91×10^{-3}	2.70×10^{-4}	6.34×10^{-4}
butadiene	5.91	6.03	1.03×10^{-2}	1.03×10^{-2}	2.52×10^{-3}	3.71×10^{-3}
cyclopentadiene	4.49	4.53	6.87×10^{-3}	6.95×10^{-3}	5.63×10^{-4}	9.22×10^{-4}
cytosine	2.97	3.71	1.51×10^{-3}	4.95×10^{-3}	2.27×10^{-2}	4.30×10^{-2}
ethene	7.22	6.99	1.98×10^{-3}	1.99×10^{-3}	6.18×10^{-4}	8.35×10^{-4}
formaldehyde	3.51	3.31	1.87×10^{-3}	1.89×10^{-3}	5.43×10^{-4}	9.23×10^{-4}
formamide	4.48	4.33	2.86×10^{-3}	2.82×10^{-3}	1.15×10^{-3}	1.59×10^{-3}
furan	5.97	6.10	7.53×10^{-3}	7.56×10^{-3}	5.10×10^{-4}	7.76×10^{-4}
hexatriene	4.99	5.07	7.25×10^{-3}	7.19×10^{-3}	1.41×10^{-3}	2.25×10^{-3}
imidazole	0.04	0.01	4.24×10^{-2}	9.81×10^{-2}	1.03×10^{-2}	1.58×10^{-2}
naphthalene	4.38	4.40	1.44×10^{-3}	1.51×10^{-3}	3.67×10^{-4}	5.30×10^{-4}
norbornadiene	2.38	2.28	4.70×10^{-3}	4.94×10^{-3}	2.51×10^{-3}	3.55×10^{-3}
octatetraene	4.34	4.41	5.19×10^{-3}	5.14×10^{-3}	1.16×10^{-3}	1.70×10^{-3}
propanamide	4.60	4.46	3.00×10^{-3}	2.98×10^{-3}	1.85×10^{-3}	2.88×10^{-3}
pyrazine	3.82	3.66	1.94×10^{-3}	1.94×10^{-3}	2.59×10^{-4}	4.69×10^{-4}
pyridazine	3.05	2.88	8.42×10^{-3}	8.01×10^{-3}	1.10×10^{-3}	1.75×10^{-3}
pyridine	4.01	3.85	3.66×10^{-3}	3.63×10^{-3}	1.36×10^{-3}	2.01×10^{-3}
pyrimidine	3.46	3.31	2.11×10^{-3}	2.11×10^{-3}	3.27×10^{-4}	5.18×10^{-4}
pyrrole	0.08	0.07	8.90×10^{-4}	1.92×10^{-3}	4.89×10^{-2}	6.83×10^{-2}
tetrazine	2.02	1.83	1.06×10^{-3}	1.12×10^{-3}	1.48×10^{-4}	2.16×10^{-4}
thymine	3.71	3.61	4.74×10^{-3}	4.68×10^{-3}	9.07×10^{-4}	1.55×10^{-3}
triazine	2.97	2.91	2.85×10^{-3}	3.12×10^{-3}	3.28×10^{-2}	4.80×10^{-2}
uracil	3.60	3.50	4.76×10^{-3}	5.29×10^{-3}	2.74×10^{-3}	4.40×10^{-3}
coronene	3.20	3.21	1.28×10^{-3}	1.37×10^{-3}	7.70×10^{-5}	1.15×10^{-4}
coumarin 153	3.05	3.05	1.50×10^{-3}	1.49×10^{-3}	1.13×10^{-1}	1.45×10^{-1}
$\mathrm{m}1^a$	3.15	3.09	3.63×10^{-3}	4.00×10^{-3}	8.05×10^{-4}	1.02×10^{-3}
Indigo	1.86	1.85	1.08×10^{-3}	9.70×10^{-4}	1.02×10^{-3}	1.67×10^{-3}
naphtacene	2.47	2.50	1.61×10^{-3}	1.69×10^{-3}	7.20×10^{-5}	1.18×10^{-4}
phtalocyanine	2.25	2.24	1.36×10^{-3}	1.46×10^{-3}	1.08×10^{-4}	1.67×10^{-4}
$\mathrm{m}2^b$	2.74	2.74	1.69×10^{-3}	1.70×10^{-3}	2.28×10^{-2}	2.98×10^{-2}

^a Norm of excited-state gradients evaluated at geometries optimized by the other method (unit in Hartree/Bohr).

^b Mean absolute difference (MAD) and root-mean-square (RMS) difference between geometries by TDA and TDA-ris (unit in Bohr).

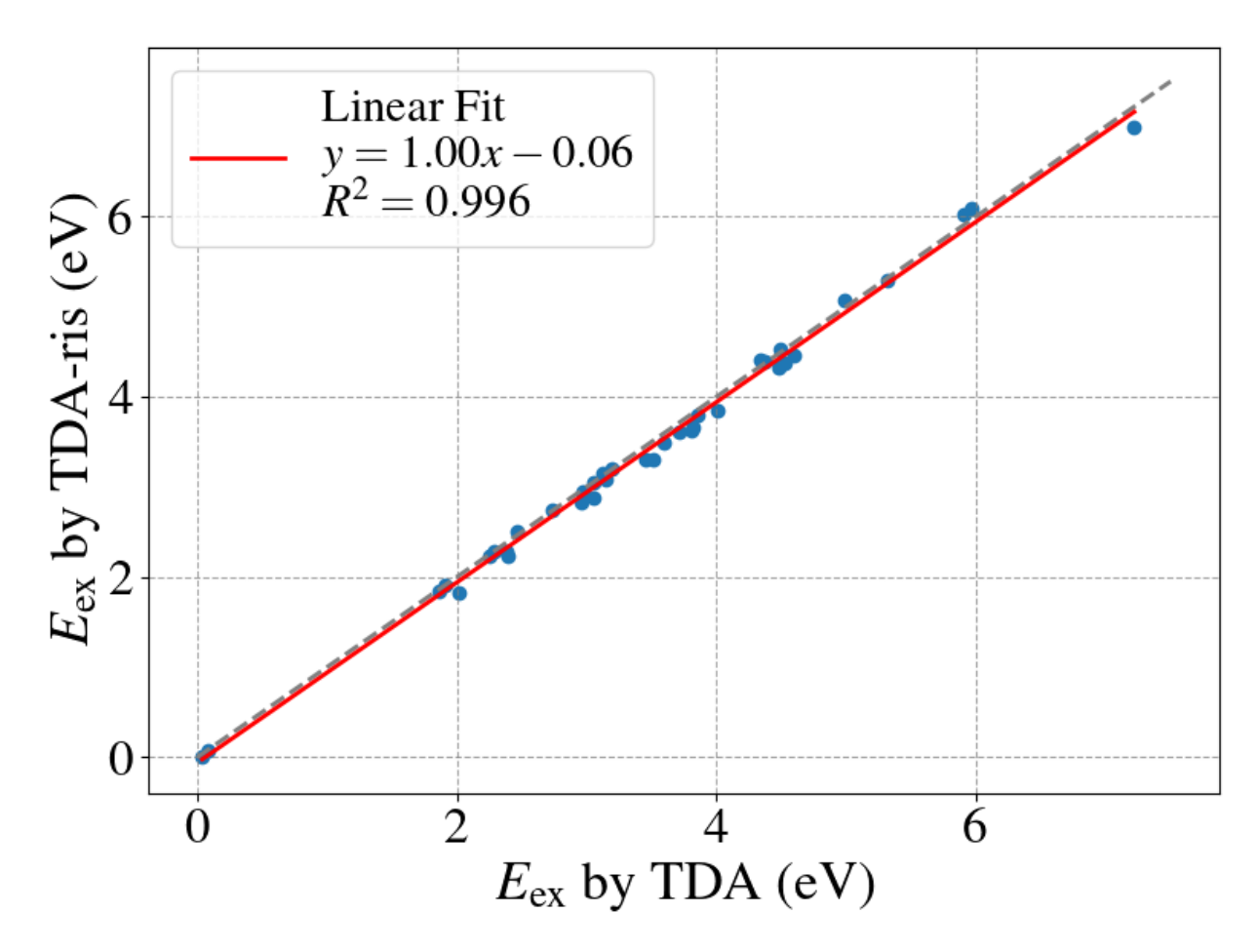


Figure 3 Vertical emission energies (in eV) computed with the TDA-ris method versus the TDA method. For each data point, both the geometry optimization and the energy calculation are performed at the corresponding level of theory. The complete emission energies are presented in Table 4. The dashed line indicates perfect agreement (y = x), and the solid red line represents the linear regression fit.

5.2 derivative coupling

Derivative couplings are fundamental quantities for modeling non-adiabatic molecular dynamics [9, 27, 50]. The test set includes a subset of molecules with geometries adopted from Ref. 61. Table 5 summarizes the MAD and RMS deviation of derivative couplings computed using the TDA-ris method against reference TDA values. The analysis encompasses couplings between the ground state (S_0) and the first excited state (S_1) , denoted as g_{01}^{ξ} , and between the S_1 and the second excited state (S_2) , denoted as g_{12}^{ξ} . As an illustration, Figure 4 depicts the derivative coupling vectors for azulene at its ground-state equilibrium geometry. Specifically, Figure 4a compares the g_{01}^{ξ} vectors, while Figure 4b presents the corresponding comparison for the g_{12}^{ξ} vectors.

The results in Table 5 indicate that the g_{01}^{ξ} couplings calculated with TDA-ris exhibit excellent agreement with the reference TDA values. In contrast, the agreement for couplings between excited states, g_{12}^{ξ} , is significantly less accurate. This trend is illustrated for azulene in Figure 4. The g_{01}^{ξ} vectors computed by both methods are nearly identical. In contrast, the g_{12}^{ξ} vectors are aligned in direction but show a larger difference in magnitude, indicating larger deviations in the TDA-ris wavefunctions for the higher excited states.

For certain molecules, significant discrepancies are observed in the derivative couplings g_{12}^{ξ} . Cytosine, for example, exhibits a significant deviation. The MAD and RMS deviations for g_{12}^{ξ} between the TDA and TDA-ris methods are 21.7 and 50.1 a_0^{-1} , respectively. This deviation can be attributed to the discrepancy in the predicted energies of the S_1 and S_2 states between the two methods. The reference TDA calculation predicts a near-degeneracy between the S_1 and S_2 states, with energies of 4.930 eV and 4.932 eV, respectively. The TDA-ris method, in contrast, predicts a larger energy gap, with corresponding energies of 4.865 eV and 4.896 eV. In the expression for the derivative coupling, the energy difference between the coupled electronic states appears in the denominator. Consequently, the small denominator arising from the small energy gap in the reference TDA calculation results in a substantially larger derivative coupling magnitude compared to that from the TDA-ris method. For comparison, the MAD and RMS deviations for the numerator term (the non-adiabatic coupling vector) of the derivative couplings are merely 1.2×10^{-4} and 3.2×10^{-4} Hartree/ a_0^{-1} , respectively. Similar large discrepancies for molecules such as cyclopentadiene, ethene, furan, and triazine also arise from this same issue.

Furthermore, the electronic structure of an excited state, as characterized by its transition vector, may differ between the TDA-ris and TDA methods. This discrepancy leads to differences in the numerator of the derivative coupling vector. When such differences in the numerator (originating from the transition vector) are compounded by small energy gaps in the denominator (due to near-degeneracy of electronic states), significant deviations between the results of the two methods will be anticipated. These issues are also manifested in the calculation of the hopping probabilities, as detailed in the subsequent section. Consequently, scenarios involving near-degenerate states, state reordering, or substantial disparities in the excited-state electronic structures between the TDA and TDA-ris formalisms must be treated with caution. Such conditions can severely compromise the accuracy of derivative coupling calculated using the TDA-ris method.

5.3 Minimum-Energy Crossing Point

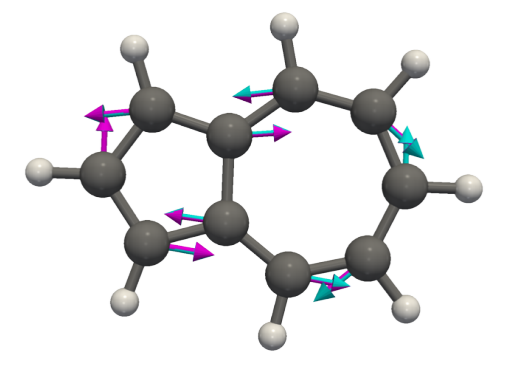
A Minimum-Energy Crossing Point (MECP) is the molecular configuration of lowest energy on the crossing seam where the potential energy surfaces of two or more electronic states are degenerate [50, 82]. In the vicinity of an MECP, the electronic degeneracy is lifted by infinitesimal geometric distortions within the branching plane. This plane is determined by two vectors: the derivative coupling vector and the gradient-difference vector ($\mathbf{x}_1 = \mathbf{g}_J^\xi - \mathbf{g}_I^\xi$). Locating an MECP requires optimization algorithms that utilize both of these vectors. The search for an MECP resembles the geometry optimization of an excited state, with the distinction that it necessitates the evaluation of derivative coupling vectors in addition to nuclear gradients. Following the procedure detailed in Ref. 5, the effective gradient \tilde{g} is defined as

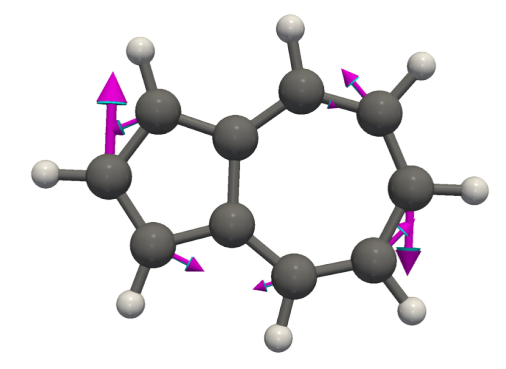
$$\widetilde{\boldsymbol{g}} = \boldsymbol{f} + \boldsymbol{g},\tag{28}$$

where $\mathbf{f} = (E_J - E_I) \frac{\mathbf{x_1}}{|\mathbf{x_1}|}$ is the gradient component that minimizes the energy difference between the S_J and S_I states. The second term, $\mathbf{g} = P\mathbf{g}_J^{\xi}$, is the gradient of the S_J state, projected by the operator P onto the orthogonal complement of the plane spanned by $\mathbf{x_1}$ and \mathbf{g}_{IJ}^{ξ} , which serves to locate the lowest energy point

Table 5 Comparison of derivative couplings for $S_0 - S_1$ and $S_1 - S_2$ using TDA and TDA-ris methods (unit in a_0^{-1}).

Molecule	S_0	-S ₁	S_1 - S_2		
Molecule	MAD	RMS	MAD	RMS	
acetamide	8.74×10^{-4}	1.58×10^{-3}	9.73×10^{-3}	1.60×10^{-2}	
acetone	5.31×10^{-4}	8.13×10^{-4}	2.74×10^{-3}	4.06×10^{-3}	
adenine	6.23×10^{-4}	1.35×10^{-3}	2.36×10^{-2}	6.26×10^{-2}	
azulene	7.06×10^{-4}	1.23×10^{-3}	4.57×10^{-3}	8.60×10^{-3}	
benzene	1.57×10^{-3}	2.38×10^{-3}	6.85×10^{-3}	9.93×10^{-3}	
benzoquinone	3.86×10^{-4}	1.08×10^{-3}	5.22×10^{-2}	9.76×10^{-2}	
butadiene	2.20×10^{-3}	3.63×10^{-3}	2.17×10^{-2}	3.63×10^{-2}	
cyclopentadiene	1.45×10^{-3}	2.61×10^{-3}	5.58×10^{-3}	9.97×10^{-3}	
cyclopropene	1.14×10^{-3}	2.55×10^{-3}	5.21×10^{-1}	1.05	
cytosine	9.57×10^{-4}	1.47×10^{-3}	2.17×10^{1}	5.01×10^{1}	
ethene	3.27×10^{-4}	6.94×10^{-4}	3.42×10^{-1}	7.25×10^{-1}	
formaldehyde	6.50×10^{-4}	1.59×10^{-3}	8.11×10^{-3}	1.67×10^{-2}	
formamide	8.75×10^{-4}	2.01×10^{-3}	6.09×10^{-3}	1.43×10^{-2}	
furan	1.51×10^{-3}	2.74×10^{-3}	1.60	3.13	
hexatriene	1.52×10^{-3}	2.59×10^{-3}	5.57×10^{-3}	9.53×10^{-3}	
imidazole	1.08×10^{-3}	2.17×10^{-3}	4.63×10^{-2}	7.85×10^{-2}	
naphthalene	6.82×10^{-4}	9.28×10^{-4}	8.97×10^{-2}	1.78×10^{-1}	
norbornadiene	9.25×10^{-4}	1.90×10^{-3}	2.69×10^{-2}	4.20×10^{-2}	
octatetraene	1.11×10^{-3}	1.73×10^{-3}	2.93×10^{-3}	4.97×10^{-3}	
propanamide	6.94×10^{-4}	1.35×10^{-3}	7.32×10^{-3}	1.36×10^{-2}	
pyrazine	6.58×10^{-4}	1.16×10^{-3}	7.23×10^{-2}	1.39×10^{-1}	
pyridazine	9.99×10^{-4}	2.07×10^{-3}	9.53×10^{-2}	1.95×10^{-1}	
pyridine	6.48×10^{-4}	1.39×10^{-3}	2.02×10^{-1}	4.15×10^{-1}	
pyrimidine	1.10×10^{-3}	2.12×10^{-3}	1.45×10^{-1}	2.99×10^{-1}	
pyrrole	8.13×10^{-4}	2.17×10^{-3}	6.01×10^{-3}	1.26×10^{-2}	
tetrazine	4.78×10^{-4}	1.28×10^{-3}	4.24×10^{-2}	7.97×10^{-2}	
thymine	3.38×10^{-4}	6.90×10^{-4}	8.16×10^{-3}	1.66×10^{-2}	
triazine	3.30×10^{-5}	8.14×10^{-5}	6.03	1.06×10^{1}	
uracil	5.16×10^{-4}	1.11×10^{-3}	4.00×10^{-3}	8.97×10^{-3}	





- (a) Coupling between the S_0 and S_1 states.
- **(b)** Coupling between the S_1 and S_2 states.

Figure 4 Derivative couplings for azulene. The vectors derived from the TDA and TDA-ris methods are depicted as magenta and cyan arrows, respectively, illustrating the coupling between the (a) S_0/S_1 (g_{01}^{ξ}) and (b) S_1/S_2 (g_{12}^{ξ}) electronic states.

on the crossing seam. The resulting effective gradients are then supplied to geometry optimization routines to locate the MECP.

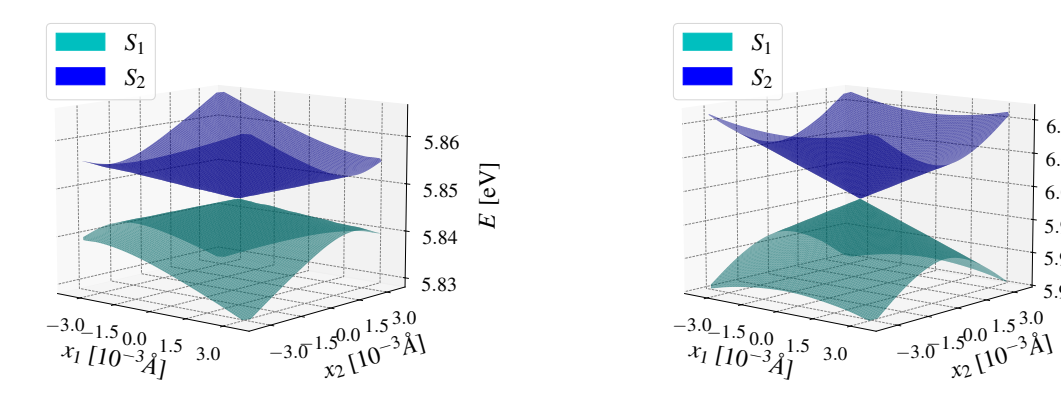
We use the furan molecule as a test system and apply both the TDA and TDA-ris methods to locate the MECP between the S_1 and S_2 states. Figure 5 compares the MECP geometries optimized using the two methods. The geometries obtained from TDA (pink) and TDA-ris (red) are highly similar. The TDA-ris method yields an MECP geometry that is structurally analogous to that obtained from the standard TDA method, exhibiting only minor discrepancies.

Using these optimized geometries, the potential energy surfaces of the S_1 and S_2 states are plotted within their respective branching planes, as shown in Figure 6a (TDA) and Figure 6b (TDA-ris). The overall topology of the potential energy surfaces near the MECP is comparable for both methods. Subtle differences in structural details are observed. A primary distinction lies in the absolute energy of the crossing seam. The TDA-ris method (Figure 6b) places the MECP at approximately 5.998 eV, representing a significant upward energy shift compared to the 5.847 eV predicted by the standard TDA calculation (Figure 6a). Furthermore, the local topographies of the potential energy surfaces differ in their symmetry. The standard TDA result exhibits a pronounced anisotropy within the branching plane; the surface is relatively flat along one diagonal, with an energy difference of only 0.015 eV between its endpoints, but exhibits a much steeper gradient along the orthogonal diagonal, with an energy difference of 0.036 eV. In contrast, the TDA-ris method yields a more isotropic potential energy surface, where the energy variation is more uniform across the surface, resulting in a comparable energy difference of approximately 0.025 eV along both diagonals.

Despite these discrepancies in absolute energy and surface topography, the fundamental geometric structure of the MECP is qualitatively conserved between the two methods. Both calculations robustly predict a well-defined conical intersection, which is the essential feature governing non-adiabatic transitions at this point of degeneracy. This suggests that while the finer quantitative details of the potential energy landscape are sensitive to the chosen computational approach, the core physical feature of the S_1 - S_2 state crossing is reliably captured by both TDA and TDA-ris. This finding, combined with the results for emission energies (Figure 3), confirms the suitability of the TDA-ris method for describing potential energy surface properties, including the equilibrium geometries of excited states and their intersections.



Figure 5 The geometry of the S_1/S_2 minimum energy crossing point of furan using TDA (pink atoms) and TDA-ris (red atoms).



6.010

6.005 6.000 \(\sum_{\text{\tint{\text{\tint{\text{\tinit}\\ \text{\texi}\text{\text{\texi}\text{\text{\text{\texi{\text{\texi{\texi{\texi{\texi}\text{\texit{\texi}\texi{\texi{\texi{\texi{\texi{\texi{\texi{\texi{\texi{\tex{

5.990

5.995 E

(a) TDA potential energy surface in the branching plane (b) TDA-ris potential energy surface in the branching plane

Figure 6 Potential energy surfaces within the branching plane of the S_1/S_2 minimum energy crossing point of furan, determined using (a) the TDA and (b) the TDA-ris methods, respectively.

5.4 Hopping Possibilities in Fewest Switches Surface Hopping Simulations

Another application of non-adiabatic couplings is the calculation of hopping probabilities in FSSH algorithm. To evaluate the applicability of the TDA-ris method in this context, we examine the time-derivative non-adiabatic coupling matrix element, T_{IJ} . This term is proportional to the FSSH transition probability and is defined as $T_{IJ} = g_{IJ}^{\xi} \cdot v$, where v denotes the nuclear velocity vector [27]. Consequently, the T_{IJ} values computed using the TDA-ris method are compared with those obtained from the reference TDA method. Formaldehyde, ethene, acetone, and hexatriene are selected as test molecules. For each molecule, a set of initial conditions (geometries and velocities) is generated via Wigner sampling [49, 77] to compute the T_{IJ} values. Based on initial structures from Ref. 61, 30 geometries are sampled at 300 K and are provided in the Supporting Information. The correlation between the results from the two methods is illustrated in Figures 7 to 10.

The results reveal significant performance variations contingent upon the coupled electronic states and molecules under consideration. For the derivative coupling between the ground state (S_0) and the first excited state (S_1) , denoted as $\boldsymbol{g}_{01}^{\xi}$, and that between the first (S_1) and second (S_2) excited states, $\boldsymbol{g}_{12}^{\xi}$, the TDA and TDA-ris methods generally exhibit a strong linear correlation. However, the $\boldsymbol{g}_{01}^{\xi}$ coupling in ethene (Figures 8a) and the $\boldsymbol{g}_{12}^{\xi}$ coupling in both formaldehyde and ethene (Figure 7b and 8b) are notable exceptions to this trend. The correlation line deviates significantly from the ideal y = x line.

The deviations can be attributed to two factors. First, for certain systems, there are significant systematic discrepancies in the excitation energy gaps predicted by the TDA and TDA-ris methods. This discrepancy introduces a scaling factor in the denominator of the derivative coupling expression, which amplifies the error in the coupling vectors, as discussed in Section 5.2. The g_{12}^{ξ} couplings for formaldehyde and ethene fall into this category. This factor is directly responsible for the deviation of the correlation slope from 1.0, as shown in Figures 7b and 8b.

A second cause for the particularly poor linear correlation observed for ethene stems from a more fundamental issue. This discrepancy originates from an intrinsic limitation of the TDA-ris approach, arising from the differences in the excited-state electronic structures (i.e., transition vectors) computed by the TDA and TDA-ris methods at certain molecular geometries. For instance, across the sampled geometries of ethene, the maximum discrepancies in the components of \mathbf{g}_{01}^{ξ} between the two methods span a wide range, from 0.0017 to 0.0200 a_0^{-1} . In contrast, this range is considerably narrower for hexatriene, spanning from 0.0093 to 0.0097 a_0^{-1} . Such a large variation for ethene leads to the observed poor linear correlation. This discrepancy in the computed excited-state electronic structure causes substantial deviations in the numerator (the non-adiabatic coupling vector) of the derivative coupling. The combination of this numerator error with significant deviations in the denominator (the excitation energy gap) results in both a poor linear correlation and a slope that deviates from the ideal y = x line (Figure 8b).

The present results suggest that the TDA-ris scheme might not always be a robust approximation for general FSSH applications. Therefore, we strongly recommend a preliminary validation similar to the tests presented here before applying the TDA-ris method to other systems. However, for systems where the relevant states and couplings exhibit strong agreement with the reference TDA results (e.g., acetone and hexatriene examined in this study), the TDA-ris method can be employed with greater confidence.

6 Conclusion

In this work, we present an implementation of excited-state gradients and derivative couplings for the TDDFT-ris framework based on the standard TDDFT formalism and program infrastructure. We examine the TDDFT-ris method with respect to standard TDDFT in terms of its computational performance and accuracy for applications involving excited-state potential energy surfaces and excited-state dynamics.

Our benchmarks indicate that for calculations pertinent to excited-state dynamics, the TDDFT-ris approximation provides a moderate enhancement in performance, achieving an overall acceleration of approximately two- to three-fold. In terms of accuracy, TDDFT-ris generally yields reasonable results for properties such as optimized geometries and excitation energies when compared to standard TDDFT. However, the inherent

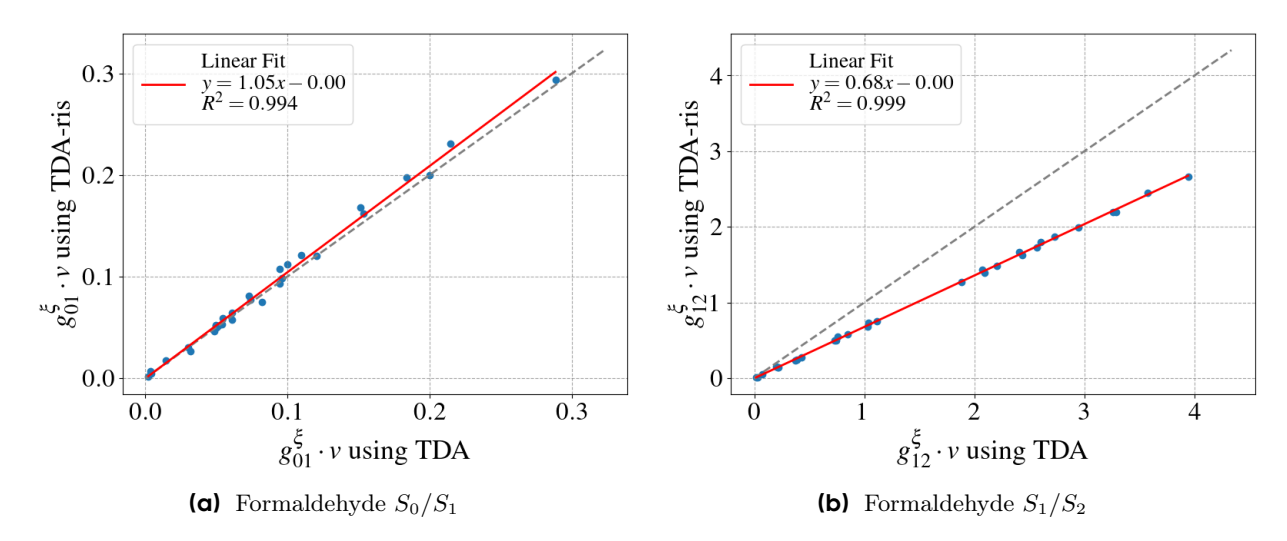


Figure 7 Correlation of time-derivative non-adiabatic coupling matrix elements $(T_{IJ} = \mathbf{g}_{IJ}^{\xi} \cdot \mathbf{v})$ from TDA and TDA-ris calculations for formaldehyde.

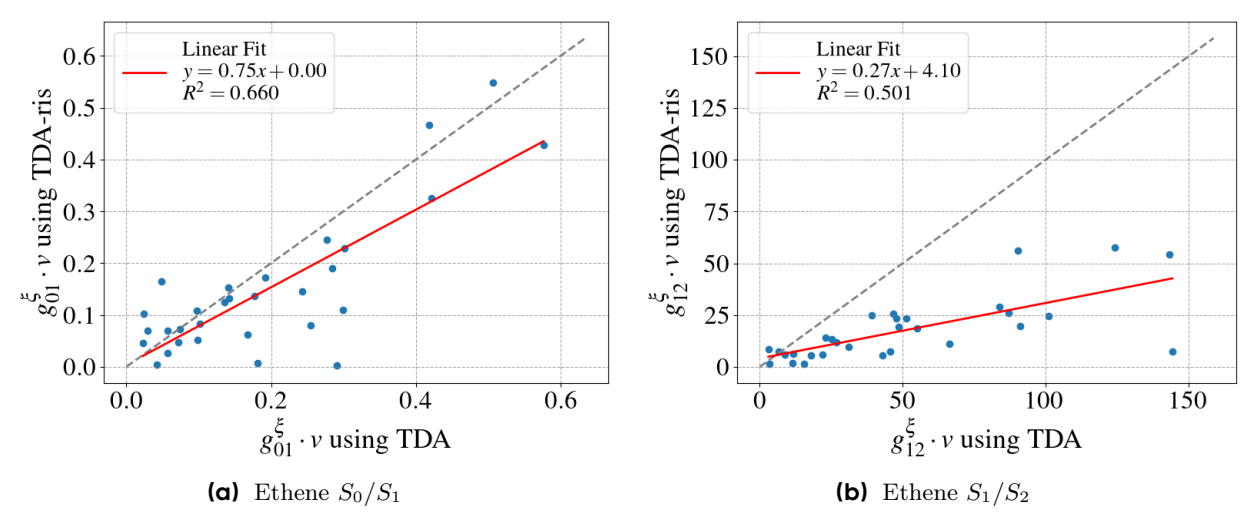


Figure 8 Correlation of time-derivative non-adiabatic coupling matrix elements from TDA and TDA-ris calculations for ethene.

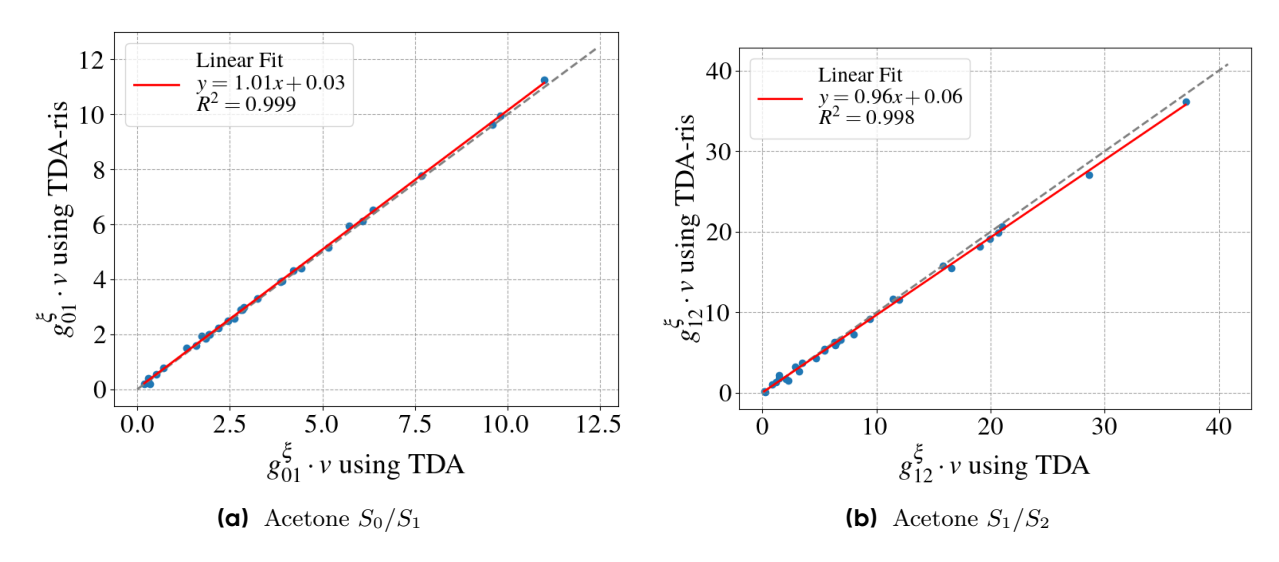


Figure 9 Correlation of time-derivative non-adiabatic coupling matrix elements from TDA and TDA-ris calculations for acetone.

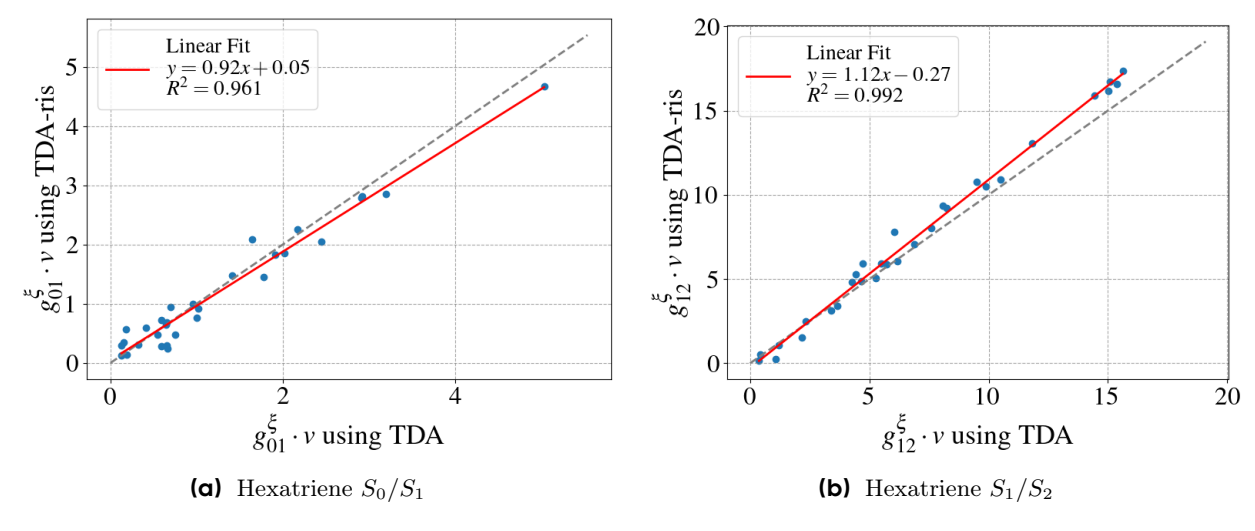


Figure 10 Correlation of time-derivative non-adiabatic coupling matrix elements from TDA and TDA-ris calculations for hexatriene.

errors in the TDDFT-ris excitation energies and electronic structures, relative to TDDFT, can be amplified during the calculation of derivative couplings. This phenomenon is particularly pronounced in the evaluation of transition probabilities, where significant deviations are observed for certain systems and electronic states. Furthermore, the energetic ordering of excited states in TDDFT-ris calculations may differ from that in standard TDDFT, which can complicate the interpretation of results.

Consequently, TDDFT-ris, in its current formulation, is not recommended as a general-purpose, "black-box" tool for excited-state dynamics, as its reliable application requires considerable user expertise. Fortunately, its viability for a specific application can be proactively assessed. Prior to commencing a full-scale dynamics simulation, one can perform preliminary benchmark calculations on the system of interest—such as determining emission energies, locating MECP, or evaluating time-derivative non-adiabatic coupling matrices—to gauge whether the TDDFT-ris approach exhibits sufficient accuracy for the target calculation.

The computational efficiency and certain functionalities of the TDDFT-ris framework could be further improved, which we plan to address in future works. First, solving the Z-vector equations is the primary bottleneck in derivative calculations. Applying approximations to the Z-vector equations, analogous to those used in TDDFT-ris, could potentially accelerate this step by an order of magnitude without loss of accuracy. Additionally, TDDFT-ris inherits the well-known limitations of standard TDDFT for computing derivative couplings between the ground and excited states [34]. Approaches such as spin-flip TDDFT[23, 34, 35, 52, 85] could be extended to the TDDFT-ris framework to address these deficiencies.

7 Acknowledgment

The author, Zhichen Pu, would like to express his gratitude to Zikuan Wang and Yunlong Xiao for valuable discussions.

References

- [1] Carlo Adamo and Vincenzo Barone. Toward reliable density functional methods without adjustable parameters: The pbe0 model. The Journal of chemical physics, 110(13):6158–6170, 1999.
- [2] Christoph Bannwarth and Stefan Grimme. A simplified time-dependent density functional theory approach for electronic ultraviolet and circular dichroism spectra of very large molecules. Computational and Theoretical Chemistry, 1040:45–53, 2014.
- [3] Christoph Bannwarth, Sebastian Ehlert, and Stefan Grimme. Gfn2-xtb—an accurate and broadly parametrized self-consistent tight-binding quantum chemical method with multipole electrostatics and density-dependent dispersion contributions. Journal of chemical theory and computation, 15(3):1652–1671, 2019.
- [4] Oscar Baseggio, Giovanna Fronzoni, and Mauro Stener. A new time dependent density functional algorithm for large systems and plasmons in metal clusters. The Journal of Chemical Physics, 143(2), 2015.
- [5] Michael J Bearpark, Michael A Robb, and H Bernhard Schlegel. A direct method for the location of the lowest energy point on a potential surface crossing. Chemical physics letters, 223(3):269–274, 1994.
- [6] Mark E Casida. Time-dependent density functional response theory for molecules. In Recent Advances In Density Functional Methods: (Part I), pages 155–192. World Scientific, 1995.
- [7] Jeremy P Coe. Analytic gradients for selected configuration interaction. <u>Journal of Chemical Theory and</u> Computation, 19(3):874–886, 2023.
- [8] Jeremy P Coe. Analytic non-adiabatic couplings for selected configuration interaction via approximate degenerate coupled perturbed hartree–fock. Journal of Chemical Theory and Computation, 19(22):8053–8065, 2023.
- Basile FE Curchod and Todd J Martínez. Ab initio nonadiabatic quantum molecular dynamics. <u>Chemical reviews</u>, 118(7):3305-3336, 2018.
- [10] Pierpaolo D'Antoni, Daniele Toffoli, and Mauro Stener. Damped linear response tddft with range-separated functionals and density fitting. The Journal of Physical Chemistry A, 129(40):9453-9463, 2025. doi: 10.1021/acs.jpca.5c03798. URL https://doi.org/10.1021/acs.jpca.5c03798. PMID: 41004144.
- [11] Marc de Wergifosse and Stefan Grimme. The exact integral simplified time-dependent density functional theory (xstd-dft). The Journal of Chemical Physics, 160(20), 2024.
- [12] Gonzalo Diaz Miron, Carlos R Lien-Medrano, Debarshi Banerjee, Marta Monti, Bálint Aradi, Michael A Sentef, Thomas A Niehaus, and Ali Hassanali. Non-adiabatic couplings in surface hopping with tight binding density functional theory: The case of molecular motors. <u>Journal of Chemical Theory and Computation</u>, 20(23):10602–10614, 2024.
- [13] Shirin Faraji, Spiridoula Matsika, and Anna I Krylov. Calculations of non-adiabatic couplings within equation-of-motion coupled-cluster framework: Theory, implementation, and validation against multi-reference methods. The Journal of chemical physics, 148(4), 2018.
- [14] Ignacio Fdez Galvan, Mickael G Delcey, Thomas Bondo Pedersen, Francesco Aquilante, and Roland Lindh. Analytical state-average complete-active-space self-consistent field nonadiabatic coupling vectors: Implementation with density-fitted two-electron integrals and application to conical intersections. <u>Journal of Chemical Theory</u> and Computation, 12(8):3636–3653, 2016.
- [15] Leon Freitag, Yingjin Ma, Alberto Baiardi, Stefan Knecht, and Markus Reiher. Approximate analytical gradients and nonadiabatic couplings for the state-average density matrix renormalization group self-consistent-field method. <u>Journal of chemical theory and computation</u>, 15(12):6724–6737, 2019.
- [16] Filipp Furche. On the density matrix based approach to time-dependent density functional response theory. <u>The</u> Journal of Chemical Physics, 114(14):5982–5992, 2001.
- [17] Filipp Furche and Reinhart Ahlrichs. Adiabatic time-dependent density functional methods for excited state properties. The Journal of chemical physics, 117(16):7433–7447, 2002.
- [18] Jürgen Gauss and John F Stanton. Analytic gradients for the coupled-cluster singles, doubles, and triples (ccsdt) model. The Journal of chemical physics, 116(5):1773–1782, 2002.

- [19] Giulia Giannone and Fabio Della Sala. Minimal auxiliary basis set for time-dependent density functional theory and comparison with tight-binding approximations: Application to silver nanoparticles. The Journal of Chemical Physics, 153(8), 2020.
- [20] Stefan Grimme. A simplified tamm-dancoff density functional approach for the electronic excitation spectra of very large molecules. The Journal of chemical physics, 138(24), 2013.
- [21] Nicholas C Handy and Henry F Schaefer III. On the evaluation of analytic energy derivatives for correlated wave functions. The Journal of chemical physics, 81(11):5031–5033, 1984.
- [22] Shana Havenridge, Robert Rüger, and Christine M Aikens. Analytical excited state gradients for time-dependent density functional theory plus tight binding (tddft+ tb). The Journal of Chemical Physics, 158(22), 2023.
- [23] John M Herbert and Aniket Mandal. Spin-flip tddft for photochemistry. In <u>Time-dependent density functional theory</u>, pages 361–404. Jenny Stanford Publishing, 2022.
- [24] John M Herbert, Xing Zhang, Adrian F Morrison, and Jie Liu. Beyond time-dependent density functional theory using only single excitations: Methods for computational studies of excited states in complex systems. <u>Accounts</u> of chemical research, 49(5):931–941, 2016.
- [25] So Hirata and Martin Head-Gordon. Time-dependent density functional theory within the tamm-dancoff approximation. Chemical Physics Letters, 314(3-4):291–299, 1999.
- [26] P. Hohenberg and W. Kohn. Inhomogeneous electron gas. Phys. Rev., 136:B864-B871, Nov 1964. doi: 10.1103/PhysRev.136.B864. URL https://link.aps.org/doi/10.1103/PhysRev.136.B864.
- [27] Amber Jain and Aarti Sindhu. Pedagogical overview of the fewest switches surface hopping method. ACS omega, 7(50):45810–45824, 2022.
- [28] Inkoo Kim, Daun Jeong, Won-Joon Son, Hyung-Jin Kim, Young Min Rhee, Yongsik Jung, Hyeonho Choi, Jinkyu Yim, Inkook Jang, and Dae Sin Kim. Kohn-sham time-dependent density functional theory with tamm-dancoff approximation on massively parallel gpus. npj Computational Materials, 9(1):81, 2023. ISSN 2057-3960. doi: 10.1038/s41524-023-01041-4. URL https://doi.org/10.1038/s41524-023-01041-4.
- [29] Inkoo Kim, Daun Jeong, Leah P. Weisburn, Alexandra Alexiu, Troy Van Voorhis, Young Min Rhee, Won-Joon Son, Hyung-Jin Kim, Jinkyu Yim, Sungmin Kim, Yeonchoo Cho, I nkook Jang, Seungmin Lee, and Dae Sin Kim. Very-large-scale gpu-accelerated nuclear gradient of time-dependent density functional theory with tamm-dancoff approximation and range-separated hybrid functionals. <u>Journal of Chemical Theory and Computation</u>, 20(20): 9018–9031, 2024. doi: 10.1021/acs.jctc.4c01003. URL https://doi.org/10.1021/acs.jctc.4c01003.
- [30] Walter Kohn and Lu Jeu Sham. Self-consistent equations including exchange and correlation effects. Phys. Rev., 140(4A):A1133, 1965.
- [31] Susi Lehtola, Conrad Steigemann, Micael J.T. Oliveira, and Miguel A.L. Marques. Recent developments in libxc—a comprehensive library of functionals for density functional theory. SoftwareX, 7:1-5, 2018. ISSN 2352-7110. doi: https://doi.org/10.1016/j.softx.2017.11.002. URL https://www.sciencedirect.com/science/article/pii/S2352711017300602.
- [32] Susi Lehtola, Conrad Steigemann, Micael JT Oliveira, and Miguel AL Marques. Recent developments in libxc—a comprehensive library of functionals for density functional theory. SoftwareX, 7:1–5, 2018.
- [33] Byron H Lengsfield, Paul Saxe, and David R Yarkony. On the evaluation of nonadiabatic coupling matrix elements using sa-mcscf/ci wave functions and analytic gradient methods. i. The Journal of chemical physics, 81(10): 4549–4553, 1984.
- [34] Benjamin G Levine, Chaehyuk Ko, Jason Quenneville, and Todd J MartÍnez. Conical intersections and double excitations in time-dependent density functional theory. Molecular Physics, 104(5-7):1039–1051, 2006.
- [35] Hao Li, Zhichen Pu, Qiming Sun, Yi Qin Gao, and Yunlong Xiao. Noncollinear and spin-flip tddft in multicollinear approach. Journal of Chemical Theory and Computation, 19(8):2270–2281, 2023.
- [36] Rui Li, Qiming Sun, Xing Zhang, and Garnet Kin-Lic Chan. Introducing gpu acceleration into the python-based simulations of chemistry framework. The Journal of Physical Chemistry A, 129(5):1459–1468, 2025.
- [37] Zhendong Li and Wenjian Liu. First-order nonadiabatic coupling matrix elements between excited states: A lagrangian formulation at the cis, rpa, td-hf, and td-dft levels. The Journal of chemical physics, 141(1), 2014.

- [38] Zhendong Li, Bingbing Suo, and Wenjian Liu. First order nonadiabatic coupling matrix elements between excited states: Implementation and application at the td-dft and pp-tda levels. The Journal of chemical physics, 141(24), 2014.
- [39] Hans Lischka, Michal Dallos, Péter G Szalay, David R Yarkony, and Ron Shepard. Analytic evaluation of nonadiabatic coupling terms at the mr-ci level. i. formalism. <u>The Journal of chemical physics</u>, 120(16):7322-7329, 2004.
- [40] Sebastian Mai, Felix Plasser, Mathias Pabst, Frank Neese, Andreas Köhn, and Leticia González. Surface hopping dynamics including intersystem crossing using the algebraic diagrammatic construction method. The Journal of Chemical Physics, 147(18), 2017.
- [41] Ericka Roy Miller, Sean J Hoehn, Abhijith Kumar, Dehua Jiang, and Shane M Parker. Ultrafast photochemistry and electron diffraction for cyclobutanone in the s2 state: Surface hopping with time-dependent density functional theory. The Journal of Chemical Physics, 161(3), 2024.
- [42] Carolin Müller, Štěpán Sršeň, Brigitta Bachmair, Rachel Crespo-Otero, Jingbai Li, Sascha Mausenberger, Max Pinheiro Jr, Graham Worth, Steven A Lopez, and Julia Westermayr. Machine learning for nonadiabatic molecular dynamics: best practices and recent progress. Chemical Science, 2025.
- [43] Thomas A Niehaus. Approximate time-dependent density functional theory. <u>Journal of Molecular Structure:</u> THEOCHEM, 914(1-3):38–49, 2009.
- [44] Thomas A Niehaus. Ground-to-excited derivative couplings for the density functional-based tight-binding method: semi-local and long-range corrected formulations. Theoretical Chemistry Accounts, 140(4):34, 2021.
- [45] Thomas A Niehaus. Exact non-adiabatic coupling vectors for the time-dependent density functional based tight-binding method. The Journal of Chemical Physics, 158(5), 2023.
- [46] Thomas A Niehaus, S Suhai, F Della Sala, P Lugli, Marcus Elstner, Gotthard Seifert, and Th Frauenheim. Tight-binding approach to time-dependent density-functional response theory. Physical Review B, 63(8):085108, 2001.
- [47] Qi Ou, Gregory D Bellchambers, Filipp Furche, and Joseph E Subotnik. First-order derivative couplings between excited states from adiabatic tddft response theory. The Journal of chemical physics, 142(6), 2015.
- [48] Shane M Parker and Colin J Schiltz. Surface hopping with cumulative probabilities: Even sampling and improved reproducibility. The Journal of Chemical Physics, 153(17), 2020.
- [49] Jiawei Peng, Yu Xie, Deping Hu, Likai Du, and Zhenggang Lan. Treatment of nonadiabatic dynamics by on-the-fly trajectory surface hopping dynamics. Acta Phys.-Chim. Sin, 35(1):28–48, 2019.
- [50] Antonio Prlj, Jack T Taylor, Jiří Janoš, Petr Slavíček, Federica Agostini, and Basile FE Curchod. Best practices for nonadiabatic molecular dynamics simulations. <u>arXiv preprint arXiv:2508.05263</u>, 2025.
- [51] Zhichen Pu and Qiming Sun. Enhancing pyscf-based quantum chemistry simulations with modern hardware, algorithms, and python tools. arXiv preprint arXiv:2506.06661, 2025.
- [52] Zhichen Pu, Hao Li, Ning Zhang, Hong Jiang, Yiqin Gao, Yunlong Xiao, Qiming Sun, Yong Zhang, and Sihong Shao. Noncollinear density functional theory. Physical Review Research, 5(1):013036, 2023.
- [53] Dmitrij Rappoport and Filipp Furche. Analytical time-dependent density functional derivative methods within the ri-j approximation, an approach to excited states of large molecules. The Journal of chemical physics, 122(6), 2005.
- [54] Dirk R Rehn and Andreas Dreuw. Analytic nuclear gradients of the algebraic-diagrammatic construction scheme for the polarization propagator up to third order of perturbation theory. The Journal of Chemical Physics, 150 (17), 2019.
- [55] Dario Rocca, Ralph Gebauer, Yousef Saad, and Stefano Baroni. Turbo charging time-dependent density-functional theory with lanczos chains. The Journal of Chemical Physics, 128(15), 2008.
- [56] Robert Rüger, Erik Van Lenthe, Thomas Heine, and Lucas Visscher. Tight-binding approximations to time-dependent density functional theory—a fast approach for the calculation of electronically excited states. The Journal of chemical physics, 144(18), 2016.

- [57] Erich Runge and Eberhard KU Gross. Density-functional theory for time-dependent systems. Physical review letters, 52(12):997, 1984.
- [58] Ilya G. Ryabinkin, Jayashree Nagesh, and Artur F. Izmaylov. Fast numerical evaluation of time-derivative nonadiabatic couplings for mixed quantum-classical methods. J. Phys. Chem. Lett., 6(21):4200–4203, November 2015. doi: 10.1021/acs.jpclett.5b02062. URL https://doi.org/10.1021/acs.jpclett.5b02062.
- [59] Eduarda Sangiogo-Gil, Lea M. Ibele, Richard Bleyer, and Leticia González. Velocity rescaling in surface hopping based on atomic contributions to electronic transitions. J. Chem. Theory Comput., 21(17):8278–8290, September 2025. ISSN 1549-9618. doi: 10.1021/acs.jctc.5c00737. URL https://doi.org/10.1021/acs.jctc.5c00737.
- [60] Giovanni Scalmani, Michael J Frisch, Benedetta Mennucci, Jacopo Tomasi, Roberto Cammi, and Vincenzo Barone. Geometries and properties of excited states in the gas phase and in solution: Theory and application of a time-dependent density functional theory polarizable continuum model. The Journal of chemical physics, 124(9), 2006.
- [61] Marko Schreiber, Mario R Silva-Junior, Stephan Sauer, and Walter Thiel. Benchmarks for electronically excited states: Caspt2, cc2, ccsd, and cc3. The Journal of chemical physics, 128(13), 2008.
- [62] Robert Send and Filipp Furche. First-order nonadiabatic couplings from time-dependent hybrid density functional response theory: Consistent formalism, implementation, and performance. The Journal of chemical physics, 132 (4), 2010.
- [63] John F Stanton and Jürgen Gauss. Analytic energy derivatives for ionized states described by the equation-of-motion coupled cluster method. The Journal of chemical physics, 101(10):8938-8944, 1994.
- [64] Joseph E Subotnik, Ethan C Alguire, Qi Ou, Brian R Landry, and Shervin Fatehi. The requisite electronic structure theory to describe photoexcited nonadiabatic dynamics: Nonadiabatic derivative couplings and diabatic electronic couplings. Accounts of chemical research, 48(5):1340–1350, 2015.
- [65] Joseph E Subotnik, Amber Jain, Brian Landry, Andrew Petit, Wenjun Ouyang, and Nicole Bellonzi. Understanding the surface hopping view of electronic transitions and decoherence. Annual review of physical chemistry, 67(1): 387–417, 2016.
- [66] Qiming Sun, Xing Zhang, Samragni Banerjee, Peng Bao, Marc Barbry, Nick S Blunt, Nikolay A Bogdanov, George H Booth, Jia Chen, Zhi-Hao Cui, et al. Recent developments in the pyscf program package. The Journal of chemical physics, 153(2), 2020.
- [67] Attila Tajti and Péter G Szalay. Analytic evaluation of the nonadiabatic coupling vector between excited states using equation-of-motion coupled-cluster theory. The Journal of chemical physics, 131(12), 2009.
- [68] Enrico Tapavicza, Ivano Tavernelli, and Ursula Rothlisberger. Trajectory surface hopping within linear response time-dependent density-functional theory. Physical review letters, 98(2):023001, 2007.
- [69] John C Tully. Molecular dynamics with electronic transitions. <u>The Journal of Chemical Physics</u>, 93(2):1061–1071, 1990.
- [70] John C Tully. Perspective: Nonadiabatic dynamics theory. The Journal of chemical physics, 137(22), 2012.
- [71] Samat Tussupbayev, Niranjan Govind, Kenneth Lopata, and Christopher J Cramer. Comparison of real-time and linear-response time-dependent density functional theories for molecular chromophores ranging from sparse to high densities of states. Journal of chemical theory and computation, 11(3):1102–1109, 2015.
- [72] Hiroki Uratani, Toshiki Morioka, Takeshi Yoshikawa, and Hiromi Nakai. Fast nonadiabatic molecular dynamics via spin-flip time-dependent density-functional tight-binding approach: Application to nonradiative relaxation of tetraphenylethylene with locked aromatic rings. <u>Journal of chemical theory and computation</u>, 16(12):7299–7313, 2020.
- [73] Brent Walker, A Marco Saitta, Ralph Gebauer, and Stefano Baroni. Efficient approach to time-dependent density-functional perturbation theory for optical spectroscopy. Physical review letters, 96(11):113001, 2006.
- [74] Zikuan Wang, Chenyu Wu, and Wenjian Liu. Nac-tddft: Time-dependent density functional theory for nonadiabatic couplings. Accounts of Chemical Research, 54(17):3288–3297, 2021.
- [75] Florian Weigend. Hartree–fock exchange fitting basis sets for h to rn. <u>Journal of computational chemistry</u>, 29(2): 167–175, 2008.

- [76] Florian Weigend and Reinhart Ahlrichs. Balanced basis sets of split valence, triple zeta valence and quadruple zeta valence quality for h to rn: Design and assessment of accuracy. Physical Chemistry Chemical Physics, 7(18): 3297–3305, 2005.
- [77] Eugene Wigner. On the quantum correction for thermodynamic equilibrium. Physical review, 40(5):749, 1932.
- [78] Fangqin Wu, Wenjian Liu, Yong Zhang, and Zhendong Li. Linear-scaling time-dependent density functional theory based on the idea of "from fragments to molecule". <u>Journal of Chemical Theory and Computation</u>, 7(11): 3643–3660, 2011.
- [79] Xiaojie Wu, Qiming Sun, Zhichen Pu, Tianze Zheng, Wenzhi Ma, Wen Yan, Yu Xia, Zhengxiao Wu, Mian Huo, Xiang Li, et al. Enhancing gpu-acceleration in the python-based simulations of chemistry frameworks. Wiley Interdisciplinary Reviews: Computational Molecular Science, 15(2):e70008, 2025.
- [80] Xiaoyan Wu, Shizheng Wen, Huajing Song, Thomas Frauenheim, Sergei Tretiak, ChiYung Yam, and Yu Zhang. Nonadiabatic molecular dynamics simulations based on time-dependent density functional tight-binding method. <u>The Journal of Chemical Physics</u>, 157(8):084114, 08 2022. ISSN 0021-9606. doi: 10.1063/5.0100339. URL https://doi.org/10.1063/5.0100339.
- [81] Xiaoyan Wu, Shizheng Wen, Huajing Song, Thomas Frauenheim, Sergei Tretiak, ChiYung Yam, and Yu Zhang. Nonadiabatic molecular dynamics simulations based on time-dependent density functional tight-binding method. The Journal of Chemical Physics, 157(8), 2022.
- [82] Xiaoyu Zhang, Tai Wang, Yi Qin Gao, and Yunlong Xiao. Noncollinear spin-flip tddft for potential energy surface crossings: Conical intersections and spin crossings. <u>Journal of chemical theory and computation</u>, 0(0):null, 0. doi: 10.1021/acs.jctc.5c01272. URL https://doi.org/10.1021/acs.jctc.5c01272. PMID: 41208132.
- [83] Xing Zhang and John M Herbert. Analytic derivative couplings for spin-flip configuration interaction singles and spin-flip time-dependent density functional theory. The Journal of Chemical Physics, 141(6), 2014.
- [84] Xing Zhang and John M Herbert. Analytic derivative couplings in time-dependent density functional theory: Quadratic response theory versus pseudo-wavefunction approach. The Journal of chemical physics, 142(6), 2015.
- [85] Xing Zhang and John M Herbert. Nonadiabatic dynamics with spin-flip vs linear-response time-dependent density functional theory: A case study for the protonated schiff base c5h6nh2+. The Journal of Chemical Physics, 155 (12), 2021.
- [86] Zehao Zhou and Shane M Parker. Converging time-dependent density functional theory calculations in five iterations with minimal auxiliary preconditioning. <u>Journal of Chemical Theory and Computation</u>, 20(15):6738– 6746, 2024.
- [87] Zehao Zhou, Fabio Della Sala, and Shane M Parker. Minimal auxiliary basis set approach for the electronic excitation spectra of organic molecules. The Journal of Physical Chemistry Letters, 14(7):1968–1976, 2023.
- [88] Tim J Zuehlsdorff, Nicholas DM Hine, James S Spencer, Nicholas M Harrison, D Jason Riley, and Peter D Haynes. Linear-scaling time-dependent density-functional theory in the linear response formalism. The Journal of Chemical Physics, 139(6), 2013.

Appendix

A Appendix: Detailed Formulations for Excited-State Gradients and Derivative Couplings

This section presents the detailed formulations for the excited-state gradients and derivative couplings.

A.1 Definitions for the Generating Function

The matrices and notations that appear in Eqs. (12) to (14) are defined in Ref. 38 and are reproduced here for convenience.

$$T_{IJ} = \frac{1}{2} \left(\gamma^{IJ} (II) + \left[\gamma^{IJ} (II) \right]^T \right), \tag{29}$$

$$\gamma^{IJ}(II) = C\gamma^{IJ}(II)C^{T}, \tag{30}$$

$$\gamma_{pq}^{IJ} = \gamma_{pq}^{IJ}(II) = \begin{bmatrix} -(X_J^T X_I + Y_I^T Y_J)_{ij} & 0\\ 0 & (X_I X_J^T + Y_J Y_I^T)_{ab} \end{bmatrix}, \tag{31}$$

$$\Gamma_{IJ} = \{ \boldsymbol{R}_{I}^{S}, \boldsymbol{R}_{J}^{S} \} + \{ \boldsymbol{L}_{I}^{A}, \boldsymbol{L}_{J}^{A} \}, \tag{32}$$

$$\mathbf{R}_I^S = \frac{1}{2} (\mathbf{R}_I + \mathbf{R}_I^T), \quad \mathbf{R}_I = \mathbf{C}_V R_I \mathbf{C}_O^T, \quad R_I = X_I + Y_I,$$
 (33)

$$\boldsymbol{L}_{I}^{A} = \frac{1}{2} (\boldsymbol{L}_{I} - \boldsymbol{L}_{I}^{T}), \quad L_{I} = X_{I} - Y_{I}, \tag{34}$$

$$[\underline{d}]_{pq} = \langle p|q(x)\rangle, \tag{35}$$

$$\underline{\gamma} = C\gamma [C(x)]^T, \tag{36}$$

$$\gamma_{pq}^{0I} = \begin{bmatrix} 0 & X_{I,ai} \\ Y_{I,ai} & 0 \end{bmatrix}. \tag{37}$$

Here, boldface letters denote quantities in the atomic orbital basis, whereas plain-type letters represent quantities in the molecular orbital basis. The underline indicates that only the ket depends on the nuclear coordinate x in atomic-orbital basis. Following Ref. 38, the contraction of an integral with density matrices is denoted as

$$\langle O_n; \{D_1, D_2, \dots, D_n\} \rangle = \sum_{P_1 P_2 \dots P_n} O_{P_1 P_2 \dots P_n} (D_1)_{P_1} (D_2)_{P_2} \dots (D_n)_{P_n}, \tag{38}$$

where P_i represents a pair of molecular orbital indices, such as pq. For example, the contraction of the second term on the right-hand side of Eq. (12) reads

$$\langle \boldsymbol{g}; \boldsymbol{\Gamma}_{II} \rangle = \langle \boldsymbol{g}; \{\boldsymbol{R}_{I}^{S}, \boldsymbol{R}_{J}^{S}\} + \{\boldsymbol{L}_{I}^{A}, \boldsymbol{L}_{J}^{A}\} \rangle$$

$$= \langle \boldsymbol{g}; \boldsymbol{R}_{I}^{S}, \boldsymbol{R}_{J}^{S}\} \rangle + \langle \boldsymbol{g}; \{\boldsymbol{L}_{I}^{A}, \boldsymbol{L}_{J}^{A}\} \rangle$$

$$= \sum_{pqrs} g_{pq,rs} [\boldsymbol{R}_{I}^{S}]_{pq} [\boldsymbol{R}_{J}^{S}]_{rs} + \sum_{pqrs} g_{pq,rs} [\boldsymbol{L}_{I}^{A}]_{pq} [\boldsymbol{L}_{J}^{A}]_{rs}.$$

$$(39)$$

For detailed definitions of these terms, the reader is referred to Ref. 38.

A.2 Terms for Calculating Derivatives in Standard TDDFT

The main text presents the formulas for excited-state gradients and derivative couplings using the notation defined in Ref. 38 without detailed clarification, which is provided here for completeness. In Eqs. (15) to (18), \mathbf{H} is the matrix representing the kinetic energy and the electron-nucleus attraction, and the density-like

matrices are defined as

$$P_I = T_{II} + Z^S, (41)$$

$$\mathbf{Z}^{S} = \frac{1}{2}(\mathbf{Z} + \mathbf{Z}^{T}), \quad \mathbf{Z} = \mathbf{C}_{V} \mathbf{Z} \mathbf{C}_{O}^{T}, \tag{42}$$

$$P_{IJ} = T_{IJ} + \tilde{Z}^S, \tag{43}$$

$$\tilde{M} = (E_J - E_I)M, \quad M = Z, W, \gamma^{IJ}, L_{IJ},$$
(44)

$$\tilde{\gamma}^{IJ} = \tilde{\gamma}^{IJ}(II). \tag{45}$$

The XC potential matrix, v_{xc} , used in Eqs. (15) to (18), is defined by its matrix elements as

$$(\mathbf{v}_{\rm xc})_{pq} = \frac{\partial E_{\rm xc}}{\partial D_{qp}}.\tag{46}$$

The matrices Z and W in Eqs. (15) to (18) need to be determined. The matrix Z is determined from the Z-vector equation (19),

$$(\mathbf{A} + \mathbf{B})\mathbf{Z} = g^{(\text{VO})} - g^{(\text{OV})}, \tag{47}$$

with the definition (Eq. (41) in Ref. 38)

$$L^{(pp')} = \sum_{q} \frac{\partial L}{\partial C_{qp}(x)} C_{qp'}(x). \tag{48}$$

The matrix element $g^{(pp')}$ adopts different forms for the gradient, the derivative couplings between the ground and excited states, and the derivative couplings between different excited states. The matrix W is calculated as

$$W_{ij} = \frac{1}{2}g^{(ij)} + G_{ij}[\mathbf{Z}^S], \tag{49}$$

$$W_{ab} = \frac{1}{2}g^{(ab)},\tag{50}$$

$$W_{ia} = \frac{1}{2}g^{(ia)} + G_{ia}[\mathbf{Z}^S] + \frac{1}{2}\sum_{b} F_{ab}Z_{bi},$$
(51)

$$W_{ai} = \frac{1}{2}g^{(ai)} + \frac{1}{2}\sum_{i} Z_{aj}F_{ji}, \tag{52}$$

with the notation defined as

$$G[\mathbf{Z}^S] = \mathbf{C}^T \mathbf{G}[\mathbf{Z}^S] \mathbf{C}, \quad \mathbf{G}[\mathbf{Z}^S] = \mathbf{g}[\mathbf{Z}^S] + \mathbf{f}_{xc}[\mathbf{Z}^S].$$
 (53)

For the excited-state gradient, the matrix element $g^{(pp')}$ is calculated as

$$g_I^{(pp')} = 2\left[D(G[\boldsymbol{T}_{II}] + k_{xc}[\boldsymbol{R}_I^S, \boldsymbol{R}_I^S])\right]_{pp'} + 2\left[T_{II}F\right]_{pp'} + 4\left[R_I^SG[\boldsymbol{R}_I^S]\right]_{pp'} - 4\left[L_I^Ag[\boldsymbol{L}_I^A]\right]_{pp'},$$

$$(54)$$

where the definitions for the density matrices, from Eq. (82) in Ref. 38, are

$$D = \begin{bmatrix} I & 0 \\ 0 & 0 \end{bmatrix},\tag{55}$$

$$T_{II} = \begin{bmatrix} -\frac{1}{2} (R_I^T R_I + L_I^T L_I) & 0\\ 0 & \frac{1}{2} (R_I R_I^T + L_I L_I^T) \end{bmatrix},$$
 (56)

$$R_I^S = \begin{bmatrix} 0 & \frac{1}{2}R_I^T \\ \frac{1}{2}R_I & 0 \end{bmatrix}, \quad L_I^A = \begin{bmatrix} 0 & -\frac{1}{2}L_I^T \\ \frac{1}{2}L_I & 0 \end{bmatrix}, \tag{57}$$

$$\langle g; \{D_1, D_2\} \rangle = \langle g[D_1]; \{D_2\} \rangle = \langle g[D_2]; \{D_1\} \rangle. \tag{58}$$

In Eq. (54), k_{xc} is defined as the third-order derivatives of the XC functional with respect to the density matrix D.

For the derivative coupling between the ground state and excited state I, the matrix element $g^{(pp')}$ is defined as

$$g_{0I}^{(pp')} = \gamma_{p'p}^{0I}. (59)$$

For the derivative couplings between excited states I and J, the matrix element $g^{(pp')}$ is defined as

$$g_{IJ}^{(pp')} = (E_J - E_I)^{-1} Q_{IJ}^{(pp')} + \gamma_{p'p}^{IJ},$$

$$Q_{IJ}^{(pp')} = 2 \left[D(G[\mathbf{T}_{IJ}] + k_{xc}[\mathbf{R}_I^S, \mathbf{R}_J^S]) \right]_{pp'} + 2 \left[T_{IJ} F \right]_{pp'}$$

$$+ 2 \left[R_I^S G[\mathbf{R}_J^S] \right]_{pp'} - 2 \left[L_I^A g[\mathbf{L}_J^A] \right]_{pp'}$$

$$+ 2 \left[R_J^S G[\mathbf{R}_I^S] \right]_{pp'} - 2 \left[L_J^A g[\mathbf{L}_I^A] \right]_{pp'}.$$
(61)

A.3 Terms for calculating derivatives in TDDFT-ris

Within the TDDFT-ris framework, the matrices Z and W are determined according to Eqs. (19) and (49)-(52), respectively. However, the matrix element $g^{(pp')}$ on the right-hand side of the Z-vector equation, Eq. (19), is defined differently. For the excited-state gradient, this term is defined as:

$$g_I^{(pp')} = 2 \left[DG[\mathbf{T}_{II}] \right]_{pp'} + 2 \left[T_{II} F \right]_{pp'}$$

$$+ 4 \left[R_I^S g^{\text{ris}} [\mathbf{R}_I^S] \right]_{pp'} - 4 \left[L_I^A g^{\text{ris}} [\mathbf{L}_I^A] \right]_{pp'}.$$

$$(62)$$

For the derivative coupling between the ground state and excited state I, the matrix element $g^{(pp')}$ is defined as:

$$g_{0I}^{(pp')} = \gamma_{p'p}^{0I}. \tag{63}$$

This expression is identical to the term $g^{(pp')}$ in the standard TDDFT formulation, as shown in Eq. (59). For derivative couplings between excited states I and J, the matrix element $g^{(pp')}$ is defined as:

$$g_{IJ}^{(pp')} = (E_J - E_I)^{-1} Q_{IJ}^{(pp')} + \gamma_{p'p}^{IJ},$$

$$Q_{IJ}^{(pp')} = 2 \left[DG[\mathbf{T}_{IJ}] \right]_{pp'} + 2 \left[T_{IJ} F \right]_{pp'}$$

$$+ 2 \left[R_I^S g^{\text{ris}} [\mathbf{R}_J^S] \right]_{pp'} - 2 \left[L_I^A g^{\text{ris}} [\mathbf{L}_J^A] \right]_{pp'}$$

$$+ 2 \left[R_J^S g^{\text{ris}} [\mathbf{R}_I^S] \right]_{pp'} - 2 \left[L_J^A g^{\text{ris}} [\mathbf{L}_I^A] \right]_{pp'}.$$
(65)

Notably, the evaluation of $g^{(pp')}$ for the excited-state gradient and the derivative couplings between excited states does not require third-order derivatives of the XC functional, yet it still necessitates the computation of the four-center integrals in G.

B Appendix: Validation with Finite Differences

To validate the implementation, the analytical excited-state gradients and derivative couplings are benchmarked against numerical finite difference calculations, for which a step size of 0.001 Å is utilized.

Table 6 presents the benchmark data for the excited-state gradients. These results are obtained using both the exact algorithm and the density fitting approximation for the evaluation of two-electron integrals. The molecular geometries for this test are adopted from Ref. 61. For all molecules tested, the analytical gradients show excellent agreement with their finite-difference counterparts. The MAD and RMS deviations are consistently on the order of 10^{-6} to 10^{-5} Hartree/Bohr, thus confirming the correctness of the analytical excited-state gradient implementation.

Table 6 Comparison of analytical and numerical finite-difference gradients for the first excited state (unit in Hartree/Bohr).

Molecule	MAD	RMS
acetamide	4.53×10^{-6}	8.35×10^{-6}
acetone	4.62×10^{-6}	7.06×10^{-6}
benzene	6.73×10^{-6}	1.30×10^{-5}
butadiene	6.17×10^{-6}	1.12×10^{-5}
cyclopentadiene	7.33×10^{-6}	1.61×10^{-5}
cyclopropene	2.06×10^{-6}	3.21×10^{-6}
ethene	1.26×10^{-6}	2.52×10^{-6}
formaldehyde	1.08×10^{-6}	2.62×10^{-6}
formamide	3.77×10^{-6}	7.43×10^{-6}
furan	1.30×10^{-5}	2.85×10^{-5}
hexatriene	5.66×10^{-6}	8.92×10^{-6}
imidazole	9.14×10^{-6}	1.84×10^{-5}
pyrazine	3.35×10^{-6}	5.85×10^{-6}
pyridazine	1.14×10^{-5}	1.97×10^{-5}
pyridine	3.93×10^{-6}	8.31×10^{-6}
pyridine	9.43×10^{-6}	1.89×10^{-5}
pyrrole	8.91×10^{-6}	2.02×10^{-5}
tetrazine	1.18×10^{-5}	1.86×10^{-5}
triazine	1.55×10^{-5}	3.31×10^{-5}

The accuracy of the analytical derivative coupling implementation is benchmarked against the finite difference method, with the results presented in Table 7. Table 7 lists the MAD and RMS deviations for the derivative couplings between the ground state (S_0) and the first excited state (S_1) , denoted as $\boldsymbol{g}_{11}^{\xi}$, and between the first (S_1) and second (S_2) excited states, denoted as $\boldsymbol{g}_{12}^{\xi}$. The results demonstrate excellent agreement for both $\boldsymbol{g}_{01}^{\xi}$ and $\boldsymbol{g}_{12}^{\xi}$. This high level of accuracy is consistent for calculations employing either the exact two-electron integrals or the density fitting approximation. Deviations from the numerical reference consistently fall within the range of 10^{-7} to 10^{-4} a_0^{-1} , which strongly validates the present implementation. Although the finite difference method serves as a valuable benchmark, its application to derivative couplings requires particular caution. For molecules with degenerate or near-degenerate molecular orbitals, obtaining a consistent difference of the molecular orbital coefficients is non-trivial, rendering the numerical approach challenging [38].

Table 7 Comparison of analytical and numerical finite-difference derivative coupling (unit in a_0^{-1}).

Molecule	$\mathrm{MAD}(\boldsymbol{g}_{01}^{\xi})$	$\mathrm{RMS}(oldsymbol{g}_{01}^{\xi})$	$\mathrm{MAD}(\boldsymbol{g}_{12}^{\xi})$	$\mathrm{RMS}(\boldsymbol{g}_{12}^{\xi})$
acetamide	2.22×10^{-6}	4.35×10^{-6}	5.50×10^{-6}	1.40×10^{-5}
acetone	4.98×10^{-6}	7.83×10^{-6}	1.13×10^{-5}	1.81×10^{-5}
cyclopropene	1.56×10^{-6}	3.08×10^{-6}	2.21×10^{-5}	4.70×10^{-5}
ethene	8.57×10^{-8}	1.81×10^{-7}	5.85×10^{-7}	9.07×10^{-7}
formamide	3.90×10^{-5}	1.07×10^{-4}	1.23×10^{-5}	2.82×10^{-5}
propanamide	1.33×10^{-5}	5.42×10^{-5}	1.98×10^{-5}	5.96×10^{-5}